Cancer Cell

Article

Interrogation of endothelial and mural cells in brain metastasis reveals key immune-regulatory mechanisms

Graphical abstract

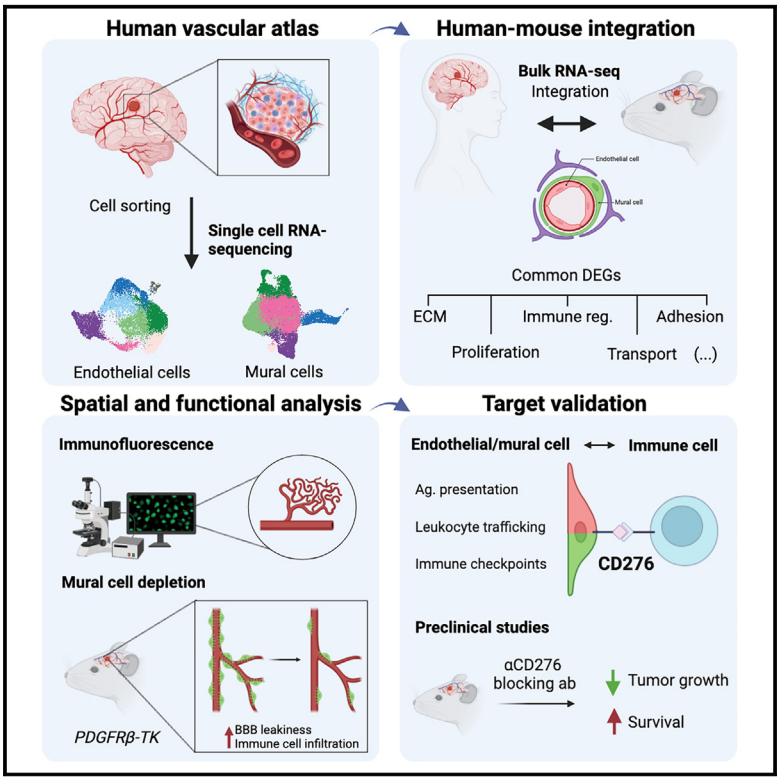

Highlights

- We performed single-cell and bulk RNA-seq of human BrM and healthy brain vascular cells
- BrMs are defined by pathological endothelial and mural cell subtypes
- We created a preclinical platform by integrating human data with mouse BrM models
- This interspecies analysis revealed CD276 as a potential therapeutic target for BrM

Authors

Leire Bejarano, Annamaria Kauzlaric, Eleni Lamprou, ..., Roy T. Daniel, Monika E. Hegi, Johanna A. Joyce

Correspondence

johanna.joyce@unil.ch

In brief

The brain tumor-associated vasculature is a key component of the tumor microenvironment in brain metastasis, protecting cancer cells from immune attack and interfering with the delivery of therapeutic agents into the brain. In this study, Bejarano et al. unravel the vascular heterogeneity in human BrM and further construct a preclinical platform to design novel vascular-targeted therapeutic strategies for the treatment of these aggressive tumors.

Bejarano et al., 2024, Cancer Cell *42*, 378–395
March 11, 2024
https://doi.org/10.1016/j.ccell.2023.12.018

CellPress

CellPress
OPEN ACCESS

Cancer Cell

Article

Interrogation of endothelial and mural cells in brain metastasis reveals key immune-regulatory mechanisms

Leire Bejarano,[1,2,3,4] Annamaria Kauzlaric,[3,5] Eleni Lamprou,[1,2,3,4] Joao Lourenco,[3,5] Nadine Fournier,[3,5] Michelle Ballabio,[1,2,3] Roberto Colotti,[6] Roeltje Maas,[1,2,3,4] Sabine Galland,[1,2,3,4] Matteo Massara,[1,2,3,4] Klara Soukup,[1,2,3] Johanna Lilja,[1,2,3] Jean-Philippe Brouland,[7] Andreas F. Hottinger,[1,4,8] Roy T. Daniel,[4,9] Monika E. Hegi,[4,9,10] and Johanna A. Joyce[1,2,3,4,11,*]

[1]Department of Oncology, University of Lausanne, Lausanne, Switzerland
[2]Ludwig Institute for Cancer Research, University of Lausanne, Lausanne, Switzerland
[3]Agora Cancer Research Centre Lausanne, Lausanne, Switzerland
[4]Lundin Family Brain Tumor Research Center, Departments of Oncology and Clinical Neurosciences, Centre Hospitalier Universitaire Vaudois, Lausanne, Switzerland
[5]Translational Data Science Facility, Swiss Institute of Bioinformatics, Lausanne, Switzerland
[6]In Vivo Imaging Facility (IVIF), University of Lausanne, Lausanne, Switzerland
[7]Department of Pathology, Centre Hospitalier Universitaire Vaudois, Lausanne, Switzerland
[8]Department of Oncology, Centre Hospitalier Universitaire Vaudois, Lausanne, Switzerland
[9]Department of Neurosurgery, Centre Hospitalier Universitaire Vaudois, Lausanne, Switzerland
[10]Neuroscience Research Center, Centre Hospitalier Universitaire Vaudois, Lausanne, Switzerland
[11]Lead contact
*Correspondence: johanna.joyce@unil.ch
https://doi.org/10.1016/j.ccell.2023.12.018

SUMMARY

Brain metastasis (BrM) is a common malignancy, predominantly originating from lung, melanoma, and breast cancers. The vasculature is a key component of the BrM tumor microenvironment with critical roles in regulating metastatic seeding and progression. However, the heterogeneity of the major BrM vascular components, namely endothelial and mural cells, is still poorly understood. We perform single-cell and bulk RNA-sequencing of sorted vascular cell types and detect multiple subtypes enriched specifically in BrM compared to non-tumor brain, including previously unrecognized immune regulatory subtypes. We integrate the human data with mouse models, creating a platform to interrogate vascular targets for the treatment of BrM. We find that the CD276 immune checkpoint molecule is significantly upregulated in the BrM vasculature, and anti-CD276 blocking antibodies prolonged survival in preclinical trials. This study provides important insights into the complex interactions between the vasculature, immune cells, and cancer cells, with translational relevance for designing therapeutic interventions.

INTRODUCTION

Brain metastasis (BrM) is the most common intracranial tumor, predominantly arising from lung cancer (40–50%), breast cancer (15–25%), and melanoma (5–20%).[1,2] Despite treatment with molecularly targeted therapies, immunotherapies, stereotactic radiosurgery, or traditional surgery,[3] median survival ranges from 5 to 10 months.[4] This underscores the need for a deep understanding of BrM biology to design more effective therapies. Recent analyses of patient samples have revealed the importance of the brain tumor microenvironment (TME) in regulating disease progression in primary and metastatic brain malignancies.[5,6] The immense complexity of the TME in BrM is being unraveled, with a particular focus to date on the immune cell landscape.[7–13] However, a similarly comprehensive atlas of the vascular compartment in human BrM is currently lacking.

The blood-brain barrier (BBB) comprises several components: endothelial cells (ECs), mural cells, astrocytic endfeet, and closely associated microglia. The tight junctions formed by ECs function as a selective barrier allowing the entrance of necessary nutrients while protecting the brain from pathogens and toxic substances.[14] However, metastasizing cancer cells can cross the BBB using different mechanisms, including proteolysis of junctional adhesion molecules,[15–17] or via transmigration.[16,18–21] After cancer cells seed and colonize the brain, including by vascular co-option,[22,23] the vasculature is also altered, forming the blood-tumor barrier.[24] While this aberrant vasculature may enable peripheral immune cell infiltration, including $CD8^+$ T cells,[7,8,11] durable immune responses do not broadly ensue. Indeed, several immune checkpoint blockade (ICB) trials showed intracranial responses in only a subset of patients with melanoma or lung cancer.[25,26]

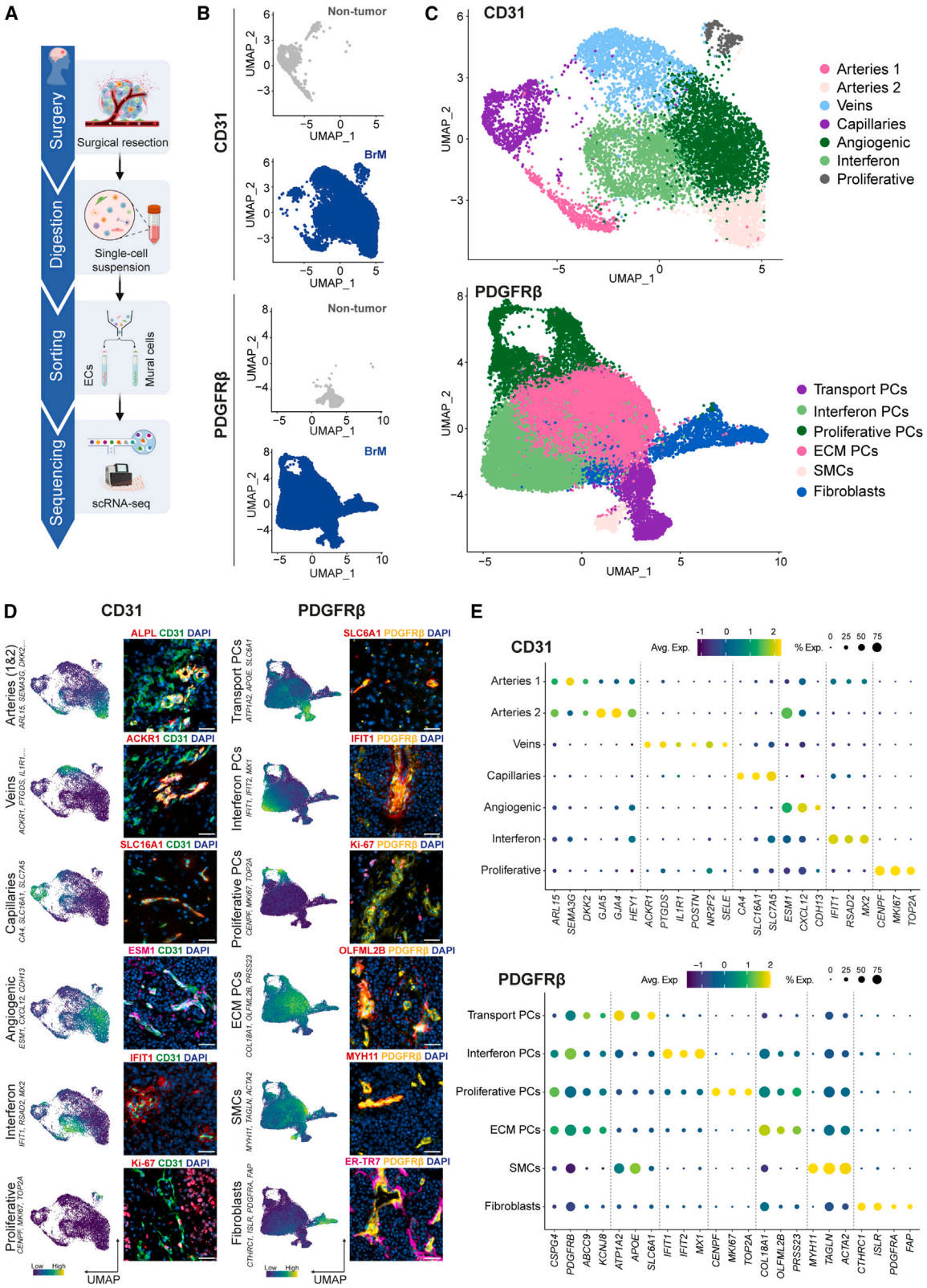

Figure 1. Taxonomy of human endothelial and mural cells in brain metastases and non-tumor samples

(A) Experimental design for clinical sample processing pipeline.

(B) UMAP plot of sorted vascular cells, color-coded for non-tumor brain (gray) and BrM (blue) samples.

(legend continued on next page)

The vasculature regulates immune cell recruitment, antigen presentation, and immune modulation in multiple organs.[27] In the brain, single-cell RNA-sequencing (scRNA-seq) of healthy and/or malformed vasculature showed considerable heterogeneity of vascular components.[28–32] However, in BrM, the vasculature has remained unexplored to this level of granularity.

To address this knowledge gap, we present an in-depth analysis of the key components of the brain tumor vasculature. We performed single-cell and bulk RNA-sequencing (RNA-seq) of vascular cells from human and mouse BrM and non-tumor brain samples, spatial TME imaging analyses, and preclinical studies using BrM models to address these questions: What is the heterogeneity of endothelial and mural cells in BrM? What are the BrM-associated structural and molecular alterations in these vascular components? How can we therapeutically target the BrM vasculature? This study provides answers to these questions through a deeper understanding of the biology of BrM, revealing effective therapeutic strategies for these aggressive tumors.

RESULTS

Endothelial and mural cell diversity in brain metastasis

To explore vascular heterogeneity in BrM, we collected fresh surgically resected tissue from six patients, including BrMs from lung or breast primary origin (five patients) and one non-tumor sample from a patient with epilepsy (Table S1). Samples were processed immediately post-surgery and single-cell suspensions subjected to fluorescence-activated cell sorting (FACS) using CD31 and PDGFRβ as markers for endothelial and mural cell isolation, respectively (Figures 1A and S1A). Following scRNA-seq and quality control filtering (Figure S1B), we obtained 10,045 and 29,798 high-quality transcriptomes from *in silico*-selected endothelial and mural cells, respectively (Figures 1B and 1C). Transcriptomes from these samples were pooled, integrated, and visualized using uniform manifold approximation and projection (UMAP) plots (Figures 1B and 1C). Sorted CD31$^+$ cells expressed EC markers (Figure S1C), while sorted PDGFRβ$^+$ cells expressed mural cell markers (Figure S1D). We did not observe expression of neuronal, astrocyte, macrophage, or cancer cell markers, confirming cellular purity (Figures S1E–S1H).

Clustering analysis revealed seven major EC populations, which were annotated using the top differentially expressed genes (DEGs) (Figures 1C–1E; Table S2). Based on described gene signatures,[33] we identified the major arteriovenous segments: "*arteries*", "*veins*", and "*capillaries*", as consistently mapping to distinct clusters within our dataset (Figures 1D, 1E, and S1I). Notably, we identified three additional clusters, termed "*angiogenic*" (*ESM1*, *CXCL12*, *CDH13*), "*interferon*" (*IFIT1*, *RSAD2*, *MX2*), and "*proliferative*" (*CENPF*, *MKI67*, *TOP2A*) based on enrichment of the indicated genes and others (Figures 1D, 1E and S1I). This was validated by immunofluorescence (IF) staining and analysis in BrM and non-tumor brain tissue samples (Figure 1D). To analyze BrM-specific alterations, we divided our dataset into non-tumor and BrM groups (Figures 2A and S2A), revealing clear differences in cluster distribution. In non-tumor tissue, the majority of cells mapped to the established arteriovenous zonation, with ~99.9% of cells distributed in clusters assigned to "*capillaries*", "*arteries*", or "*veins*" (Figure 2B). By contrast, in BrM samples, only ~36.1% of cells mapped to the arteriovenous axis, while the remaining cells mapped within the "*angiogenic*" (~37.8%), "*interferon*"(~23.6%), or "*proliferative*"(~2.5%) clusters (Figure 2B). BrM-ECs showed significant enrichment of *PLVAP,* which is involved in vascular permeability and negatively correlates with BBB integrity[34] (Figure S2B). We further validated these findings by integrating our data with publicly available single-cell data of non-tumor brain ECs.[31] Transcriptomes from the Garcia et al. study and our own datasets were pooled, integrated, and visualized using UMAP plots (Figure 2C). Both UMAP and similarity plots showed high concordance for non-tumor tissues, while our BrM samples clustered independently (Figures 2C and 2D). We queried whether the clusters in our dataset were also present in the Garcia data using *scmap*[35] (Figure S2C), revealing that ~97% of cells in the Garcia dataset mapped within the arteriovenous axis, as for our non-tumor data (Figure 2E).

To explore the functionality of each cluster, we performed over-representation analysis (ORA) based on the top-ranking genes in each cluster (Figure 2F; Table S2). Both "*arteries*" clusters 1 and 2 showed significant enrichment in cell migration pathways; while cluster 1 was characterized by a higher inferred readout of interferon signaling and antigen presentation, and cluster 2—which was more abundant in BrM samples—was enriched in angiogenic pathways. The top-ranked significant pathways in the "*veins*" cluster mostly related to protein translation, while the "*capillaries*" cluster—which was substantially reduced in BrM samples—showed significant enrichment in pathways associated with transport and response to ions. As expected, the "*angiogenic*" cluster was enriched in pathways related to VEGF signaling, extracellular matrix (ECM) remodeling, and cell migration; and the "*interferon*" cluster showed enrichment indicative of interferon signaling along with cell migration and angiogenesis-related pathways. Finally, the "*proliferative*" cluster was enriched in pathways associated with cell cycle progression and protein translation (Figure 2F). A recent study by Geldhof et al. reported immunomodulatory ECs in primary breast tumors.[36] We thus queried if these ECs shared similarities with the "*interferon*" ECs we identified in BrM. We pooled the Geldhof primary breast EC transcriptomes with breast-BrM ECs from our dataset, followed by integration and visualization using UMAP plots (Figure S2D). While breast primary and breast-BrM ECs showed a high degree of similarity (Figure S2E), we did not find any cells mapping within the "*interferon*" EC cluster in breast primary tumors (Figure S2F), indicating this is BrM-specific. A similar approach was taken to integrate our lung-BrM ECs with lung primary ECs from published datasets[37] (Figure S2G), showing high similarity between these samples (Figure S2H), but with the caveat that "*interferon*" ECs were a small percentage in lung-BrMs (Figures S2A and S2I).

(C) UMAP plot of sorted vascular cells (pooled non-tumor and BrM samples), color-coded for clusters identified by graph-based clustering. ECM = extracellular matrix, PC = pericyte, SMC = smooth muscle cell.
(D) UMAP representation and IF images of selected markers for each cell cluster. Scale bar: 50 μm.
(E) Dot plot representation showing expression of the selected representative genes defining each cell cluster. Also see Figure S1.

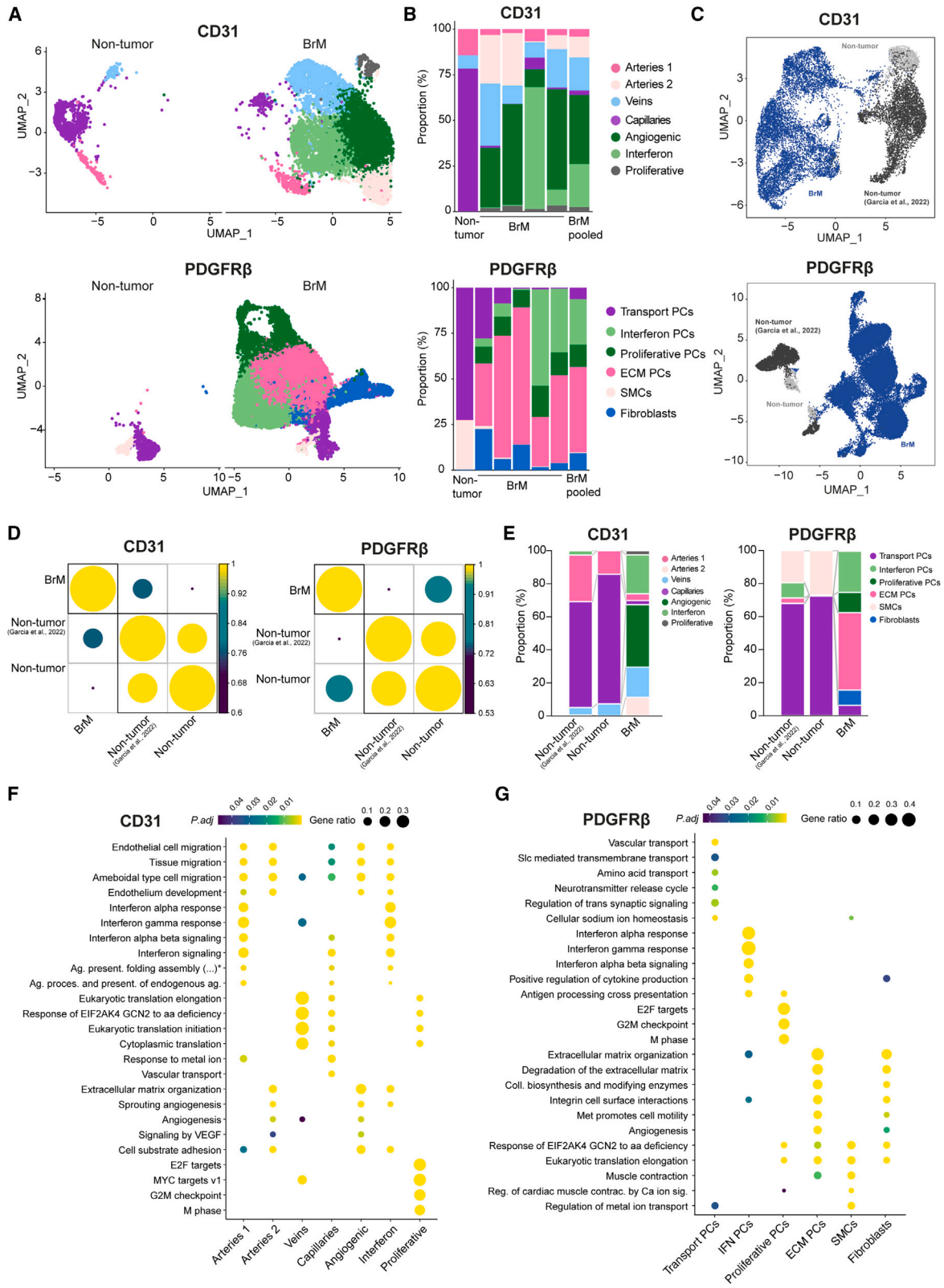

Figure 2. Brain metastases are characterized by specific pathological endothelial and mural cell clusters

(A) UMAP plots of sorted vascular cells, color-coded for identified clusters.

(B) Stacked bar graphs showing cluster proportions of each cell population.

(legend continued on next page)

Similar clustering analysis of mural cells revealed pericytes, smooth muscle cells (SMCs), and fibroblasts separating into six major clusters (Figures 1C–1E and S1I; Table S3). Pericytes represented the most abundant mural cell population, and further separated into four different clusters—"*transport*", "*interferon*", "*proliferative*", and "*ECM*"—characterized by higher expression of pericyte markers *CSPG4*, *PDGFRβ*, *ABCC9*, and *KCNJ8* (Figure 1E). The "*transport*" cluster was enriched in genes associated with the transport of ions, lipids, and other molecules (*ATP1A2*, *APOE*, and *SLC6A1*), and the "*interferon*" cluster was defined based on high expression of interferon signature genes (*IFIT1*, *IFIT2*, and *MX1*) (Figures 1D and 1E). The "*proliferative*" cluster was enriched in genes associated with cell cycle progression (*MKI67*, *CENPF*, and *TOP2A*), while the '*ECM*' cluster was characterized by genes coding for collagens, collagen-modifying enzymes, and other ECM components (*COL18A1*, *OLFML2B*, and *PRSS23*) (Figures 1D and 1E). A small subset of cells in this cluster is also high for specific SMC markers (*MYH11*, *TAGLN*, and *ACTA2)* (Figure 1D). SMCs and fibroblasts formed a single cluster, both showing high expression of the respective canonical markers, including *MYH11*, *TAGLN*, and *ACTA2* for SMCs; and *FAP*, *PDGFRA*, *CTHRC1*, and *ISLR* for fibroblasts (Figures 1D and 1E). IF analysis validated the presence of each cluster in tissue sections (Figure 1D).

Following a similar strategy to ECs, we identified BrM-specific alterations by dividing our mural cell dataset into non-tumor brain and BrM groups, revealing major differences in cluster proportions (Figure 2A). In non-tumor tissue, the major populations were "*transport*" pericytes (~72.4% of total mural cells) and SMCs (~27%) (Figures 2B and S2A). The remaining clusters represented <1% of total cells. By contrast, in BrM, "*ECM*" pericytes represented the most abundant cluster (~46.8%), followed by "*interferon*" pericytes (~24.9%)—which were highly enriched in breast-BrM samples—and "*proliferative*" pericytes (~12.2%). The less abundant populations included fibroblasts (~9.2%), "*transport*" pericytes (~6.4%), and SMCs (<1%). Notably, BrM-pericytes were significantly enriched in *THY1* (Figure S2B), which is associated with immunosuppression in malignant gliomas.[38] To validate these findings using an independent dataset, we integrated our data with the Garcia non-tumor brain mural single-cell data[31] (Figure 2C). As for the EC analyses, the Garcia non-tumor mural cells clustered closely with our non-tumor mural cells, showing high similarity (Figures 2C and 2D), while BrM-mural cells were clearly distinct. When our clusters were projected into the Garcia dataset using *scmap* (Figure S2C), we found the major populations were "*transport*" pericytes (~67.87%) and SMCs (~19.5%) (Figure 2E).

We next performed ORA based on the top-ranking genes from each cluster (Figure 2G; Table S3). "*Transport*" pericytes, the most abundant cluster in non-tumor brain samples, were enriched in pathways associated with transport of different molecules, neurotransmission, and ion homeostasis. "*Interferon*" pericytes were specifically abundant in breast-BrM samples and showed enrichment in antigen presentation, interferon signaling and response. As expected, the top significant pathways in "*proliferative*" pericytes were related to cell cycle progression and protein translation, while "*ECM*" pericytes—representing the main cluster in BrM samples—were enriched in pathways associated with ECM synthesis and modification, motility, angiogenesis, and protein translation. Fibroblasts also showed enrichment in similar pathways, while SMCs were characterized by increased protein translation, contraction, and ion transport (Figure 2G).

Endothelial and mural cell transcriptomes are altered in brain metastasis

To perform a broader investigation of the transcriptional alterations in vascular components, we collected fresh surgically resected tissue from a larger cohort of 21 individuals, including patients diagnosed with epilepsy (used as non-tumor control, 5 samples) and BrM originating from breast (5 samples), lung (8 samples), or melanoma (3 samples) primary tumors (Table S1). Tissue samples were processed using the same strategy as for scRNA-seq but instead subjected to bulk RNA-seq (Figures 3A and S1A). We confirmed the purity of the sorted cells by querying a panel of cell type-specific markers (Figure S3A).

Principal component analysis (PCA) showed that BrM-endothelial and -mural cells have very distinct transcriptional profiles compared to their non-tumor counterparts (Figure 3B). Differential expression analysis identified 840 downregulated and 641 upregulated genes when ECs were compared between BrM vs. non-tumor brain tissue (adjusted p value, $P.adj \leq 0.05$ and fold-change, FC ≥ 2) (Figure 3C; Table S4). A similar analysis for mural cells revealed 2,006 downregulated genes and 1,104 upregulated genes (Figure 3C; Table S5). We identified 207 downregulated and 200 upregulated shared DEGs between BrM-associated endothelial and mural cells (Figure 3D), suggestive of synchronized alterations under pathological conditions. Previous studies have described common vascular changes in multiple central nervous system (CNS) diseases, which are also termed the BBB dysfunction module.[39] Our analysis revealed that this module was also upregulated in both endothelial and mural cells from BrM samples, regardless of the primary tumor origin (Figures 3E and S3B). The BBB dysfunction score in ECs negatively correlated with the proportion of $CD14^+/CD16^+$ monocytes and immature myeloid cells (Figure S3C), while the mural cell score negatively correlated with lymphocyte abundance (Figure S3C).

To explore the functionality of DEGs in BrM, we performed ORA for endothelial and mural cells (Tables S4 and S5), identifying 55 downregulated and 86 upregulated shared pathways (Figure 3D). Both BrM-associated endothelial and mural cells showed significant enrichment of downregulated genes in pathways associated with transport of different substances, including organic acids, ions, or amino acids; and also with neurotransmission, cell adhesion, or cell junctions (Figures 3F, 3G, S3D, and S3E),

(C) UMAP plots of integrated vascular cells, color-coded for our dataset and public datasets.[31]
(D) Similarity plots of vascular cells comparing different datasets.
(E) Stacked bar graphs showing cluster proportions in $CD31^+$ or $PDGFR\beta^+$ populations in our dataset and public datasets.[31]
(F and G) Dotplots of selected significant pathways from ORA on DEGs in each cell cluster, including Hallmark, Reactome, and GOBP databases (cut-off: *P.adj*<0.05). *Antigen presentation folding assembly and peptide loading of class I MHC molecules. IFN = interferon. Also see Figure S2.

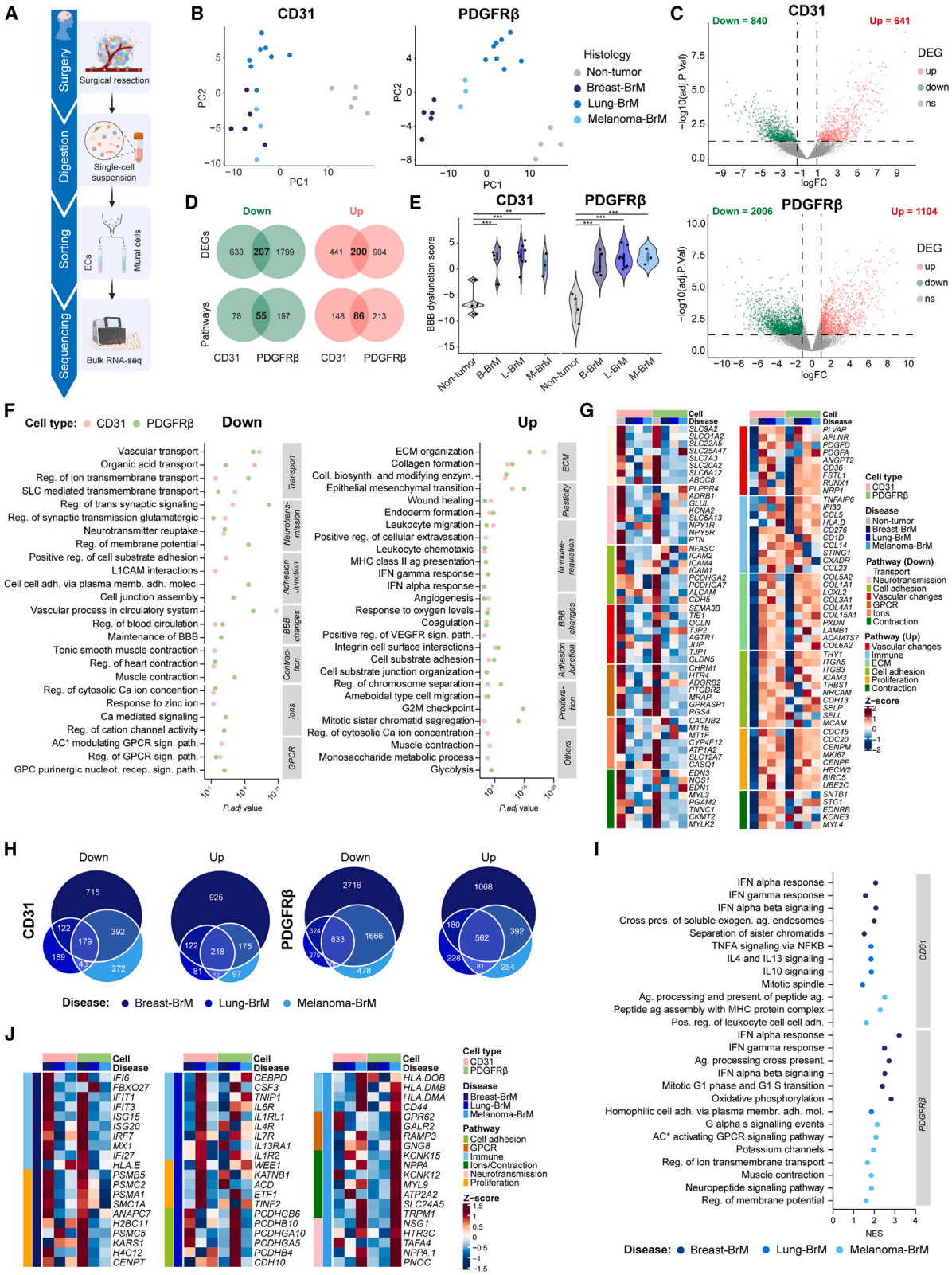

Figure 3. Endothelial and mural cell transcriptomes are altered in brain metastasis

(A) Experimental design for clinical sample processing pipeline.

(B) PCA of vascular cell transcriptional profiles in non-tumor (n_{CD31} = 5, $n_{PDGFR\beta}$ = 4) and BrM (n = 16) samples, calculated based on top 1% most variable genes.

(legend continued on next page)

suggesting an impairment in vascular homeostasis and neurovascular coupling. Consistently, additional downregulated pathways of interest are also related to BBB homeostasis, including maintenance of the BBB, and regulation of blood circulation (Figures 3F and 3G). We also found downregulated genes associated with multiple pathways involving the homeostasis, signaling, and transport of ions, regulation of G protein-coupled receptors (GPCR), and cell contraction (Figures 3F, 3G, S3D, and S3E). Notably, both ion channels and GPCR signaling play important roles in adapting blood flow to satisfy neuronal energy requirements.[40] We plotted specific genes, including *SLCO1A2* and *SLC6A13* transporters, and *NPY1R* neuropeptide, in non-tumor and BrM single-cell datasets showing these alterations occurred across the different clusters (Figures S3H and S3I).

Analysis of the upregulated genes in BrM-endothelial and -mural cells revealed pathways linked to angiogenesis, plasticity, ECM synthesis and modification (Figures 3F, 3G, S3F, and S3G), consistent with previous findings reporting collagen modification as an angiogenic pathway in lung primary tumor ECs.[37] Notably, we found upregulation of pathways related to cell adhesion, immune cell recruitment and regulation in both cell types (Figures 3F and 3G). This is consistent with recent analyses of immune landscapes in BrM, revealing diverse myeloid and lymphoid cell phenotypes.[7,8,12] Moreover, many of the top enriched pathways in BrM-mural cells were associated with proliferation and migration (Figures 3F, 3G, and S3G). This was also evident in BrM-ECs, together with increased cell contraction and calcium regulation pathways (Figures 3F, 3G, and S3F). By plotting specific genes in the non-tumor and BrM single-cell datasets, we found that several alterations occurred across every cluster, including upregulation of *ANGPT2* in both endothelial and mural cells, or *MCAM* in ECs (Figures S3H and S3I). Other genes were upregulated only in specific clusters, such as *SELP* in the "*veins*" EC cluster, *IFI30* in the "*interferon*" mural cell cluster, and *MKI67* in the "*proliferative*" cluster from both cell types (Figures S3H and S3I).

We next asked whether the primary tumor origin (i.e., breast, lung, or melanoma) influenced the vascular alterations identified in BrM. PCA showed that BrM samples originating from the same primary tumor type cluster together to some extent (Figure 3B). We compared each BrM subset independently with the non-tumor brain samples and found that while multiple DEGs were shared between all BrMs, there were also upregulated and downregulated DEGs specific to each BrM subset (Figure 3H; Tables S4 and S5). To explore primary tumor-specific changes, we performed gene set enrichment analysis (GSEA) by comparing each of the three BrM subtypes versus the two others (Figure 3I; Tables S4 and S5). We found that both endothelial and mural cells in breast-BrMs were enriched in genes and pathways related to interferon signaling and response, antigen presentation, and proliferation (Figures 3I and 3J). Lung-BrM ECs showed positive enrichment of signaling by TNFα and multiple interleukins, while lung mural cells were characterized by enriched cell adhesion molecules (Figures 3I and 3J). Lastly, melanoma-BrM ECs showed enrichment of antigen presentation and leukocyte cell adhesion-related genes and pathways, and mural cells were characterized by higher GPCR signaling, ion transport and regulation, contraction, and neurotransmission (Figures 3I and 3J).

To investigate whether the different BrM subtypes are transcriptionally similar to their corresponding primary tumors or if the metastasis site (in this case the brain) is the key determinant dictating the alterations identified, we additionally explored public datasets from breast,[41] lung,[42] and melanoma[43] primary tumors, and from glioblastoma (GBM)[44] (Figure 4A). Endothelial and mural cell from public datasets were *in silico* selected (Figures S4A–S4D), and we correlated the BrM-specific signatures—from the comparison of each BrM subtype versus the two others.

Notably, we found that both lung-BrM and breast-BrM ECs were more similar to GBM ECs, while melanoma-BrM ECs showed a higher similarity with their primary tumor counterparts (Figure 4B). When the same strategy was used for mural cells, we found again that lung-BrM mural cells were more similar to those in GBM. By contrast, both breast-BrM and melanoma-BrM mural cells showed a higher similarity to mural cells in the corresponding primary tumors (Figure 4B).

Finally, we investigated whether our bulk RNA-seq data reflected the alterations identified through the single-cell analysis (Figure 4A). We computed a signature with the top 20 DEGs from each single-cell cluster and calculated a score for all bulk RNA-seq samples (Figure 4C). For both endothelial and mural cells, the scores reflected the alterations identified by our single-cell cluster proportion analysis (Figures 2B and 4C). We next correlated the scores with immune cell proportions in each sample and found multiple significant correlations for both endothelial and mural cells (Figure 4D). For example, the "*interferon*"

(C) Volcano plot representation of DEGs in BrM vs. non-tumor samples. Horizontal and vertical dashed lines indicate $P.adj \leq 0.05$ and FC $\geq$ 2 thresholds for DEGs.

(D) Venn diagrams of DEGs and significant pathways from Hallmark, Reactome, KEGG, and GOBP databases shared between endothelial and mural cells (ORA cut-off: $P.adj<0.05$).

(E) Violin plot representation of BBB dysfunction score in vascular cells in non-tumor ($n_{CD31} = 5$, $n_{PDGFR\beta} = 4$) and BrM samples from breast (n = 5), lung (n = 8) and melanoma (n = 3) primary origin. Pair-wise comparisons using t tests with pooled SD and adjusted using Benjamini-Hochberg procedure. *P.adj* values: **p < 0.01, ***p < 0.001.

(F) Dotplot representation of selected significant pathways from Hallmark, Reactome, KEGG and/or GOBP databases on downregulated and upregulated DEGs in BrM vs. non-tumor vascular cells (ORA, cut-off: $P.adj<0.05$). *AC = Adenylate cyclase.

(G) Heatmap of selected downregulated and upregulated DEGs in BrM vs. non-tumor vascular cells.

(H) Venn diagrams of DEGs shared between breast-, lung-, and melanoma-BrM in endothelial and mural cells. DEGs calculated by comparing each BrM subtype vs. non-tumor brain (cut-off: $P.adj<0.05$, FC $\geq$ 2).

(I) Dotplot representation of selected significant pathways from GSEA vs. Hallmark, Reactome and/or GOBP databases. GSEA computed by comparing each BrM subtype vs. the two others (cut-off: $P.adj<0.05$). * AC = Adenylate cyclase.

(J) Heatmap representation of selected genes upregulated in each BrM subtype. Note: some genes may be associated with >1 pathway in (G) and (J). Also see Figure S3.

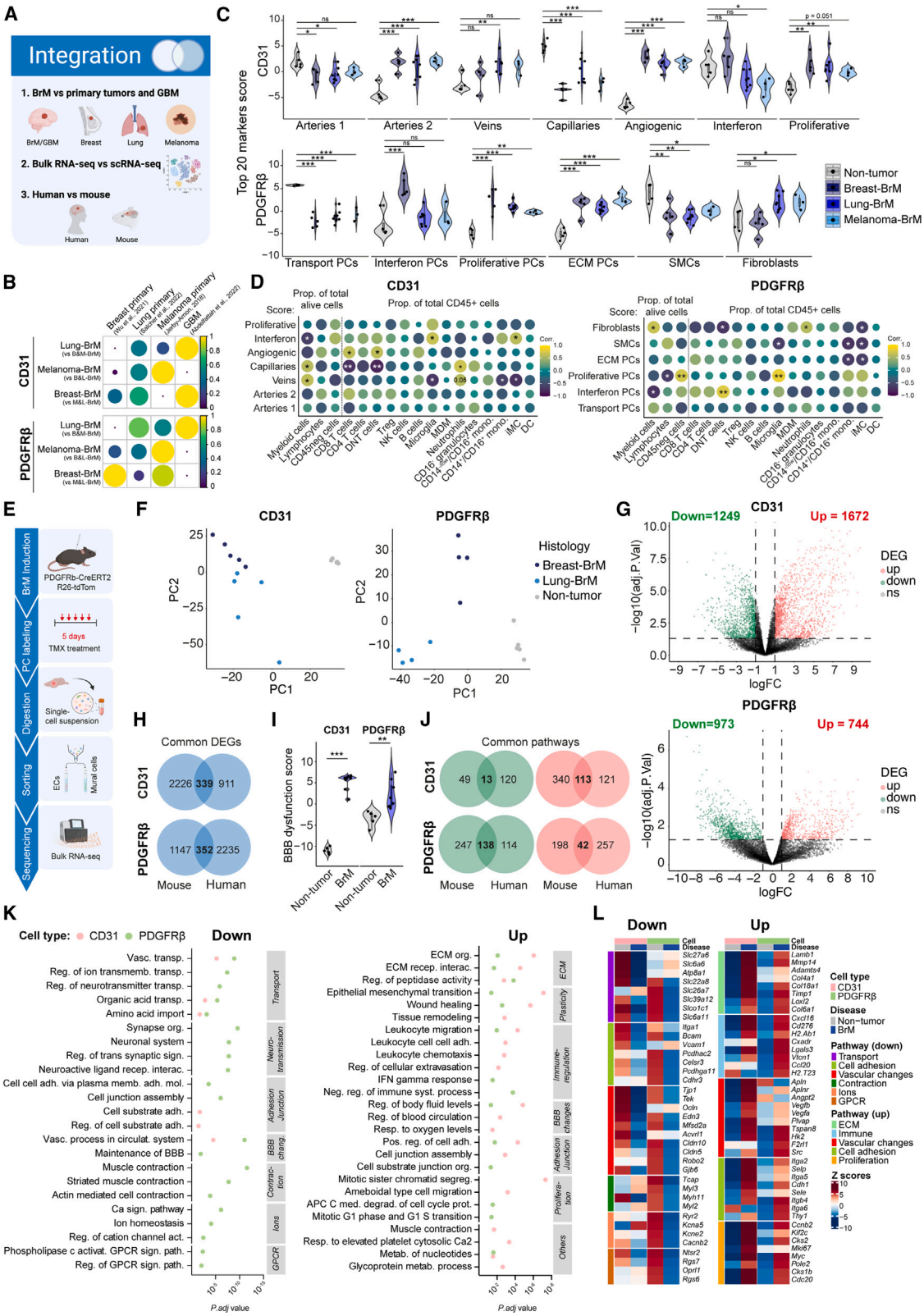

Figure 4. Integration of BrM datasets with primary tumors, GBM, and mouse datasets

(A) Experimental design for integration and different comparisons.

(B) Similarity plots comparing breast-, lung- and melanoma-BrM specific signatures with primary tumors and GBM from public datasets of human vascular cells.

(legend continued on next page)

score, which is evident in both endothelial and mural cells, negatively correlated with the proportion of myeloid cells (Figure 4D). We further validated these findings by computing additional interferon scores using gene signatures from Hallmark, Reactome, and GOBP databases, and correlating these with immune cell proportions (Figure S4E). These analyses showed that, in both endothelial and mural cells, the interferon signatures (specifically from interferon alpha and beta) negatively correlated with myeloid cell proportions and positively correlated with various T cell populations (Figure S4E).

BrM-associated vascular alterations are conserved in mouse BrM models

With the goal of identifying therapeutic targets that could be evaluated preclinically, we next addressed whether the vascular changes identified in human BrM were conserved in immune-competent mouse BrM models. We induced experimental BrM in PDGFRβ-CreERT2; Rosa-tdTomato mice[45] by intracardially injecting brain-homing cancer cells from breast (PyMT-BrM3) or lung (Sv2T3-BrM1) primary tumor origin. To label PDGFRβ-expressing cells, mice were treated with tamoxifen for 5 consecutive days as described.[45] Mice were followed by magnetic resonance imaging (MRI) and sacrificed upon developing macro-metastases. Breast- and lung-BrMs and non-tumor samples were isolated and processed immediately after resection. Single-cell suspensions were subjected to FACS, followed by bulk RNA-seq of the sorted populations (Figures 4E and S4F). We confirmed the purity of the FAC-sorted populations by plotting the same markers used in the human analyses for ECs, mural cells, neurons, astrocytes, macrophages, and cancer cells (Figure S4G).

PCA showed that mouse BrM-endothelial and -mural cells have very distinct transcriptional profiles compared to their non-tumor counterparts (Figure 4F). Differential expression analysis identified 1,249 downregulated and 1,672 upregulated genes comparing mouse BrM-ECs vs. non-tumor-brain ECs (*P.adj* $\leq$ 0.05 and FC $\geq$ 2) (Figure 4G; Table S6). Performing this comparison for mural cells revealed somewhat lower numbers of DEGs—973 downregulated and 744 upregulated genes (Figure 4G; Table S7). We performed an integration analysis of human and mouse DEGs to determine which alterations were conserved across species (Figure S4H), identifying 339 and 352 shared DEGs in endothelial and mural cells respectively (Figure 4H; Tables S6 and S7). The BBB dysfunction module was also upregulated in both endothelial and mural cells (Figures 4I and S4I). ORA on mouse DEGs revealed multiple pathways conserved between mouse and human (Figure 4J; Tables S6 and S7), including upregulation of ECM modification, proliferation, and immune cell regulation-related pathways, or downregulation of pathways associated with transport, neurotransmission, or ion homeostasis (Figures 4K and 4L). Since ECM synthesis and modification was one of the top upregulated pathways in both human and mouse samples, we validated these results by IF staining and image analysis of collagen-IV (Coll-IV) in whole tissue sections (Figures S4J–S4L).

Spatial and functional analysis of the metastatic brain tumor vasculature

We next investigated whether the transcriptional alterations identified in endothelial and mural cells were associated with structural vascular alterations by performing IF analysis using CD31 and PDGFRβ markers, respectively, in human non-tumor tissue and BrMs from breast, lung, and melanoma origin (Figure 5A). The BrM vasculature was characterized by a significant increase in vessel size (Figure 5B), most prominent in melanoma-BrMs (Figure 5B), while none of the BrM subtypes showed an increase in the total area covered by vessels (Figure S5A). In breast- and lung-BrMs, but not melanoma-BrMs, the increased vessel size was accompanied by an increased PDGFRβ$^+$ to CD31$^+$ cell ratio (Figure 5C). This was confirmed by flow cytometry analysis (Figure S5B). However, the increased PDGFRβ$^+$ to CD31$^+$ ratio did not result in increased vessel coverage by mural cells (Figure S5C). Previous studies in mice reported important roles for mural cells in regulating leukocyte trafficking during CNS homeostasis and autoimmune neuroinflammation.[46] In human BrM, we found that the extent of physical coverage of the vessels by mural cells, rather than the simple ratio of PDGFRβ$^+$ to CD31$^+$ cells, negatively correlates with the proportion of immune cells in tumors (Figures S5D and S5E).

We then asked whether these alterations were associated with a dysfunctional tumor vasculature. The presence of plasma

(C) Violin plot representation of scores calculated with top 20 markers of each cluster identified by single-cell sequencing vascular cells from non-tumor (n_{CD31} = 5, $n_{PDGFR\beta}$ = 4) and BrM samples from breast (n = 5), lung (n = 8), or melanoma (n = 3) origin. Pair-wise comparisons using t tests with pooled SD and adjusted using Benjamini-Hochberg procedure.

(D) Correlation matrices of scores computed in (C) with immune cell infiltration in different BrM samples (n = 12).

(E) Schematic of experimental BrM induction, mural cell labeling, and sample processing.

(F) PCA plots of vascular cell transcriptional profiles in non-tumor (n = 5) and BrM (n_{CD31} = 10, $n_{PDGFR\beta}$ = 8) samples, calculated based on top 10% most variable genes.

(G) Volcano plot representation of DEGs in BrM vs. non-tumor samples. Horizontal and vertical dashed lines indicate *P.adj* $\leq$ 0.05 and FC $\geq$ 2, respectively, for DEGs.

(H) Venn diagrams of shared significant DEGs between mouse and human BrM vs. non-tumor vascular cells (cut-off: *P.adj*<0.05, FC $\geq$ 2).

(I) Violin plot representation of the BBB dysfunction score in vascular cells in non-tumor (n = 5) and BrM (n_{CD31} = 10, $n_{PDGFR\beta}$ = 8). Pair-wise comparisons using t tests with pooled SD.

(J) Venn diagrams of shared significant pathways between mouse and human BrM vs. non-tumor vascular cells from Hallmark, Reactome, KEGG and GOBP databases (ORA on downregulated and upregulated genes, cut-off: *P.adj*<0.05).

(K) ORA of selected significant pathways in mouse shared with human counterparts from Hallmark, Reactome, KEGG and/or GOBP databases on downregulated and upregulated DEGs in BrM vs. non-tumor vascular cells (ORA cut-off: *P.adj*<0.05). Note that mouse pathways are only represented in dotplots if shared with human counterparts.

(L) Heatmap representation of selected downregulated and upregulated DEGs in BrM vs. non-tumor vascular cells in mouse. Note: some of these genes may be associated with >1 pathway. *P.adj* values in panel (C), p values in panels (D) and (I): *p < 0.05, **p < 0.01, ***p < 0.001, ns = non-significant. Also see Figure S4.

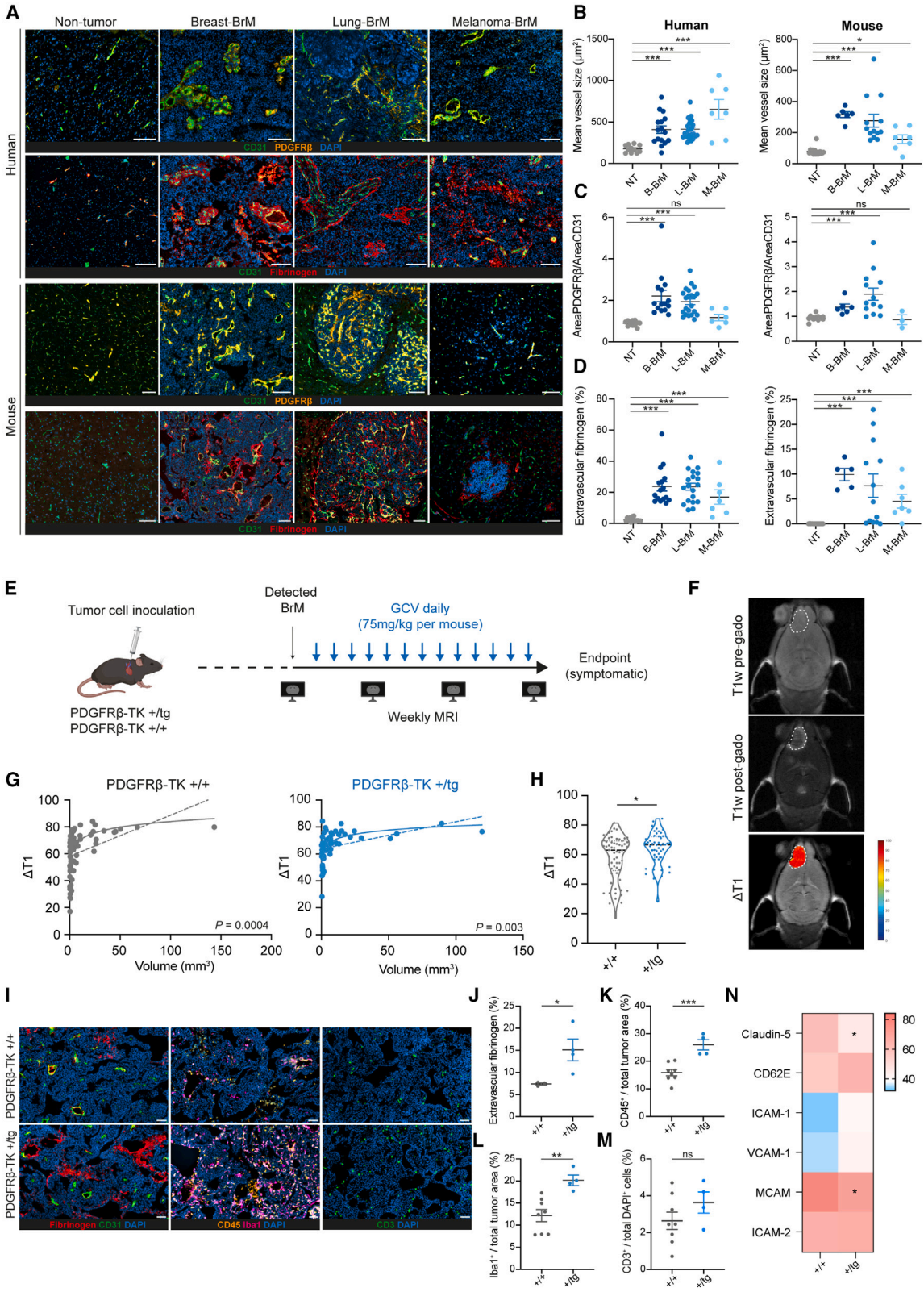

Figure 5. Brain metastasis-associated vasculature shows substantial structural and functional alterations

(A) Representative IF images of ECs, mural cells, and fibrinogen in human and mouse) non-tumor brain tissue and BrMs. Scale bar (human): 200 μm. Scale bar (mouse): 100 μm.

(legend continued on next page)

proteins, such as fibrinogen, in the brain parenchyma is indicative of a less intact, more leaky BBB.[47] We quantified extravascular fibrinogen by IF staining in BrM and non-tumor brain tissues as a readout of BBB leakiness (Figure 5A). Extravascular fibrinogen is significantly higher in human BrM from breast, lung, or melanoma origin compared to non-tumor tissue (Figure 5D). Notably, the amount of extravascular fibrinogen positively correlated with the proportion of immune cells (Figure S5F) and negatively correlated with vessel coverage by mural cells in BrMs (Figure S5G).

Similar analyses were performed in mouse BrM models induced by intracardiac injections of brain-homing cells from breast (PyMT-BrM3), lung (Sv2T3-BrM1), and melanoma (Yumm1.1-BrM4) primary tumor origin (Figure 5A), showing comparable results (Figures 5B–5D and S5A–S5C).

Mural cells regulate BBB leakiness and immune cell infiltration in brain metastasis

To explore the functions of mural cells in BrM, we used the *PDGFRβ-TK* model, which enables ganciclovir-inducible deletion of PDGFRβ-expressing cells.[48] We generated experimental BrM following intracardiac injection of PyMT-BrM3 cells in *PDGFRβ-TK* +/+ and +/*tg* mice. Upon metastasis detection by MRI, mice were treated daily with ganciclovir to deplete mural cells (Figures 5E, S5H, and S5I).

We performed a non-invasive assessment of BBB leakiness using contrast-enhanced MRI, with gadolinium as a contrast agent, where BBB leakage is calculated based on changes in T1 relaxation time values, comparing pre- vs. post-gadolinium injection (ΔT1)[49] (Figure 5F). We correlated ΔT1 values with tumor volume and found that, in both genotypes, larger metastases showed increased ΔT1 values, indicating greater BBB leakage (Figure 5G). However, the data fitted a semilogarithmic distribution, since large tumors (>approx. 15 mm^3) reached a plateau where the increase in ΔT1 was no longer observed (Figure 5G). We compared ΔT1 values in small tumors (<15 mm^3) from *PDGFRβ-TK* +/+ and +/*tg* mice and found a significant ΔT1 increase upon mural cell depletion (Figure 5H), showing that mural cells regulate BBB leakiness. We performed IF analyses in the metastatic lesions (Figure 5I), and found that mural cell-depleted BrM have increased levels of extravascular fibrinogen (Figure 5J). We also observed a positive correlation between extravascular fibrinogen and tumor area in *PDGFRβ-TK* +/+ mice (Figure S5J), underscoring that larger metastases are characterized by a leakier vasculature. This correlation was lost following mural cell depletion (Figure S5J).

We next performed IF analysis of whole tissue sections to assess the most abundant TME components in BrM, including total immune cells ($CD45^+$), tumor-associated macrophages (TAMs; $Iba1^+$), and T cells ($CD3^+$) (Figure 5I). We found that mural cell-depleted BrMs showed significant increases in $CD45^+$ cells and $Iba1^+$ cells, and a trend toward higher $CD3^+$ cell infiltration (Figures 5K–5M). To investigate which vascular changes could lead to increased immune cell infiltration we analyzed a panel of cell adhesion and tight junction molecules, including Claudin-5, CD62E, ICAM-1, VCAM-1, MCAM and ICAM-2 by IF staining (Figures 5N and S5K–S5Q). In pericyte-depleted tumors, we found a significant downregulation of Claudin-5 (Figures 5N, S5K, and S5L), consistent with a more ruptured and leaky BBB, and MCAM (Figures 5N, S5K, and S5P), reported to coordinate EC-pericyte communication.[50] We did not find significant changes in the other adhesion molecules analyzed, although there was a trend toward higher ICAM-1 and VCAM-1 in pericyte-depleted tumors (Figures 5N, S5K, S5M–S5O, and S5Q).

Molecular pathways involved in immune cell regulation by the metastatic brain tumor vasculature

To further interrogate the role of brain vascular components as immune-regulatory players we performed GSEA in BrM-endothelial and -mural cells vs. non-tumor samples in human and mouse bulk RNA-seq samples (Tables S4, S5, S6, and S7). GSEA revealed positive enrichment in multiple pathways related to immune cell regulation in both human and mouse endothelial and mural cells (Figures 6A–6D), including antigen presentation, cell adhesion, leukocyte migration, interferon signaling, and negative regulation of the immune system.

(B) Quantification of mean vessel size in human and mouse non-tumor brain tissue (n_{human} = 11, n_{mouse} = 15) and BrMs from breast (n_{human} = 16, n_{mouse} = 6), lung (n_{human} = 26, n_{mouse} = 13), and melanoma (n_{human} = 7, n_{mouse} = 7) primary origin.
(C) Quantification of PDGFRβ to CD31 ratio in human and mouse non-tumor brain (n_{human} = 11, n_{mouse} = 15) and BrMs from breast (n_{human} = 15, n_{mouse} = 6), lung (n_{human} = 22, n_{mouse} = 13), and melanoma (n_{human} = 6, n_{mouse} = 3) primary origin.
(D) Quantification of percentage of extravascular fibrinogen in human and mouse non-tumor brain (n_{human} = 15, n_{mouse} = 14) and BrMs from breast (n_{human} = 16, n_{mouse} = 5), lung (n_{human} = 19, n_{mouse} = 13), and melanoma (n_{human} = 7, n_{mouse} = 7) origin. In (B), (C) and (D), data are represented as mean ± SEM. In the human analysis, each dot represents an individual sample. In the mouse analysis, each dot represents a metastasis or group of micro-metastases for mouse melanoma-BrM. ANOVA/Kruskal-Wallis test $P_{(human)} < 0.0001$ and $P_{(mouse)} < 0.0001$ used, followed by Mann-Whitney two-tail test with Bonferroni correction method for multiple comparisons.
(E) Experimental design for BrM tumor induction, MRI monitoring, and mural cell depletion.
(F) Representative MRI images of ΔT1 quantification.
(G) Correlation of ΔT1 with tumor volume in BrMs from PDGFRβ-TK +/+ (n = 75) and +/tg (n = 57) mice. Each dot represents a metastasis. Linear and non-linear fit applied (p values from linear regression).
(H) Violin plot representation of ΔT1 in small metastasis (<15 mm^3) from PDGFRβ-TK +/+ (n = 62) and +/tg (n = 48) mice. Each dot represents a metastasis. Unpaired two-tail t test used.
(I–M) Representative IF images (I) and quantification of (J) extravascular fibrinogen, (K) immune cells ($CD45^+$), (L) macrophages ($Iba1^+$), and (M) T cells ($CD3^+$) in PDGFRβ-TK +/+ (n_J = 3, $n_{K,L,M}$ = 8) and +/tg ($n_{J,K,L,M}$ = 4) mice. Data are represented as mean ± SEM. Each dot represents a mouse. Unpaired two-tail t test used for (J)-(M). Scale bar (I): 50 μm.
(N) Heatmap representation of the percentage of ECs expressing Claudin-5, CD62E, ICAM-1, VCAM-1, MCAM and ICAM-2 in PDGFRβ-TK +/+ (n = 8) and +/tg (n = 5) mice. Mann-Whitney or unpaired two-tail t test used. *P.adj* values in panels (B-D), p values in panels (H) and (J-N): *p < 0.05, **p < 0.01, ***p < 0.001, ns = non-significant. Also see Figure S5.

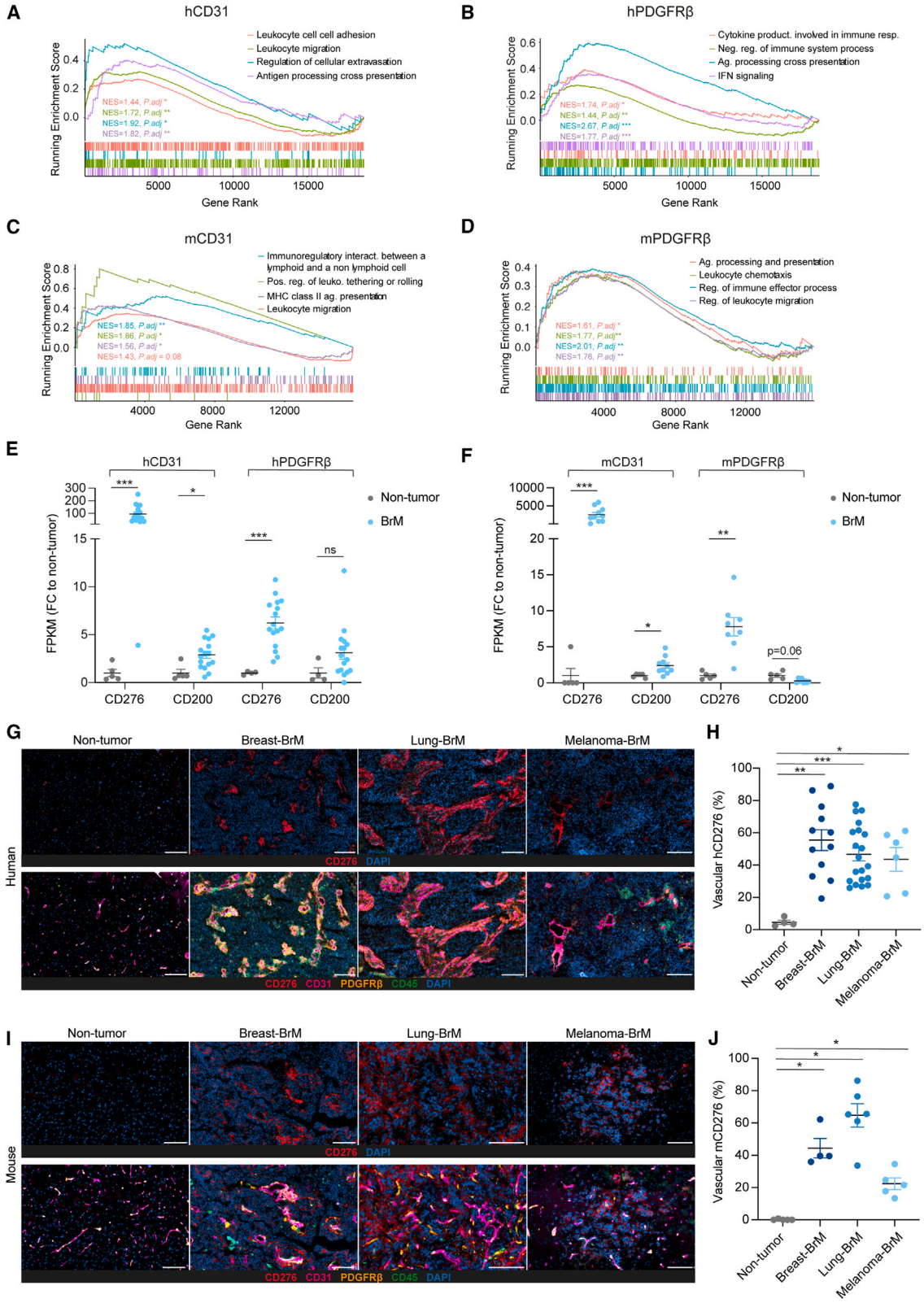

Figure 6. Molecular players involved in immune cell regulation by the tumor vasculature in mouse and human brain metastasis

(A–D) GSEA of selected immune-related gene sets from GOBP and/or Reactome databases in sorted (A) human ECs, (B) human mural cells, (C) mouse ECs, and (D) mouse mural cells (BrM vs. non-tumor, cut-off: *P.adj*<0.1).

(legend continued on next page)

We next queried whether the different vascular components may negatively regulate immune cell functions by expressing immune checkpoint molecules or T cell apoptosis drivers (Figures 6E, 6F, S6A, and S6B). Interestingly, we found that the B7-family member immune checkpoint molecule *CD276* was significantly overexpressed in both mouse and human BrM-associated endothelial and mural cells versus non-tumor samples (Figures 6E and 6F). The immune checkpoint molecule *CD200* was also significantly upregulated in human and mouse BrM-associated ECs specifically (Figures 6E and 6F). Additionally, we observed certain human or mouse-specific alterations, such as *TDO2* or *FGL1* upregulation in human BrM-mural cells or *Nectin2* and *Lgals9* upregulation in mouse BrM-EC and mural cells (Figures S6A and S6B). We also found significant alterations in several cell adhesion molecules in human and/or mouse BrM-ECs, including the downregulation of *ICAM1* and *ICAM2* in -human ECs or *Vcam1* in mouse ECs; the upregulation of *SELP* in both human and mouse BrM-ECs; and the upregulation of *Sele* in mouse ECs (Figures S6A and S6B).

Because CD276 and CD200 upregulation was conserved in both human and mouse samples, we examined these immune checkpoint molecules by IF staining in human and mouse BrM and non-tumor tissue. In human samples, CD276 expression in the tumor vasculature (defined by $CD31^+$ and/or $PDGFR\beta^+$ area) was significantly increased in BrMs from breast, lung, or melanoma primary origin (Figures 6G and 6H). To a lesser extent, we also detected an increase in non-vascular CD276 expression in BrM (Figure S6C). In BrM mouse models, we similarly found a significant upregulation of vascular CD276 in the three different models (Figures 6I and 6J). A non-vascular CD276 signal was also evident, particularly in mouse lung-BrM samples (Figure S6D). We also quantified EC-associated CD200 expression and found a significant upregulation in several human BrM samples (Figures S6E and S6F). However, this was not observed in mouse BrM models, as only very low CD200 expression was detected in breast-BrM (Figures S6G and S6H).

CD276-blocking antibodies increase survival in a mouse breast-BrM model

The B7 family member CD276 is an emerging target in cancer immunotherapy and has been reported to promote cancer cell aggressiveness and tumor angiogenesis.[51] However, CD276 has not been evaluated as a potential therapeutic target in BrM to date. Given that CD276 is upregulated in both mouse and human endothelial and mural cells, we designed a preclinical trial to evaluate the effect of a CD276-blocking antibody (MJ18). We intracardially injected PyMT-BrM3 cells in BL/6 mice and stratified the mice into isotype control or αCD276 treatment groups following BrM detection by MRI. Mice were then treated every other day with 300 μg of αCD276 or isotype control until symptoms developed (Figure 7A). Notably, αCD276 treatment led to significantly increased survival compared to isotype control-treated mice (Figures 7B and S7A–S7C). We also found a significant decrease in tumor growth two weeks after treatment (Figures 7C and 7D), indicating that CD276 may be a promising therapeutic target for BrM.

To determine whether CD276 blockade resulted in TME alterations, we performed IF analysis of the BrM-associated vasculature using fibrinogen as a readout of vessel leakiness, and a panel of cell adhesion and tight junction molecules, including Claudin-5, CD62E, ICAM-1, VCAM-1, MCAM, and ICAM-2 (Figures 7E and S7D). Notably, we found decreased extravascular fibrinogen, and increased ICAM-1 and VCAM-1, following αCD276 treatment (Figures 7F–7H). No significant changes were found in the other vascular markers analyzed (Figures S7E–S7J). Given that CD276 blockade increased cytotoxic T cell infiltration in several extracranial tumor models,[52–54] we performed IF analysis of cytotoxic T cells (Figure 7I) and found that αCD276 treatment significantly increased infiltrating $CD3^+CD8^+$ T cells in BrM (Figure 7J). We also analyzed the proportions of naive, central memory, and effector $CD8^+$ T cells, based on CD44 and CD62L levels, and the expression of several T cell activation markers including Granzyme B, Ki-67, TNFα, and IFNγ by flow cytometry (Figures 7K-L and S7K-P). αCD276-treated tumors showed a higher proportion of $CD44^+CD62L^+$ central memory and $CD44^-CD62L^+$ naive $CD8^+$ T cells (Figures 7K and S7L) and a trend toward higher $GZMB^+CD8^+$ cells (Figure 7L), but no significant changes were found in the other markers analyzed (Figures S7K and S7M-P). To explore the extent to which the therapeutic effect was mediated by T cells, we performed CD8 depletion experiments by treating the mice simultaneously with αCD276 and αCD8 antibodies, or the corresponding isotype controls, upon tumor detection by MRI. Following CD8 T cell depletion, the survival advantage conferred by αCD276 treatment was partially lost (Figure 7M), suggesting the effect is mediated by T cells, at least in part. We also investigated whether αCD276 could be combined with other immune checkpoint inhibitors, such as αPD-1, to further enhance survival. However, the dual treatment with αCD276 and αPD-1 conferred the same survival advantage as treatment with αCD276 alone (Figure 7N).

DISCUSSION

The brain tumor-associated vasculature is a crucial component of the BrM TME, protecting cancer cells from immune attack and interfering with the delivery of therapeutic agents into the brain.[55]

(E and F) Normalized counts (fragments per kilobase million, FPKM) of immune checkpoint molecules *CD276* and *CD200* in sorted (E) human and (F) mouse endothelial and mural cells. Data are represented as mean ± SEM. Each dot represents a sample. *P.adj* values from differential expression analysis by limma. (G and H) Representative IF images (G) and quantification (H) of vascular CD276 staining as a proportion of total vasculature area (vasculature area defined by $CD31^+$ and/or $PDGFR\beta^+$) in sections of human non-tumor brain tissue (n = 4) and BrMs from breast (n = 12), lung (n = 20), and melanoma (n = 6) primary origin. Scale bar (G): 200 μm.

(I and J) Representative IF images (I) and quantification (J) of vascular CD276 staining as a proportion of total vasculature area (vasculature area defined by $CD31^+$ and/or $PDGFR\beta^+$) in sections of mouse non-tumor brain tissue (n = 5) and BrMs from breast (n = 4), lung (n = 6), and melanoma (n = 5) primary origin. Scale bar (I): 100 μm. In (H) and (J) data represented as mean ± SEM. Each dot represents a sample. ANOVA/Kruskal-Wallis test $P_{(H)} = 0.007$ and $P_{(J)} = 0.001$ and Mann-Whitney two-tail test with Bonferroni correction method used. *P.adj* values in panels (A–F), (H) and (J): *p < 0.05, **p < 0.01, ***p < 0.001, ns = non-significant. Also see Figure S6.

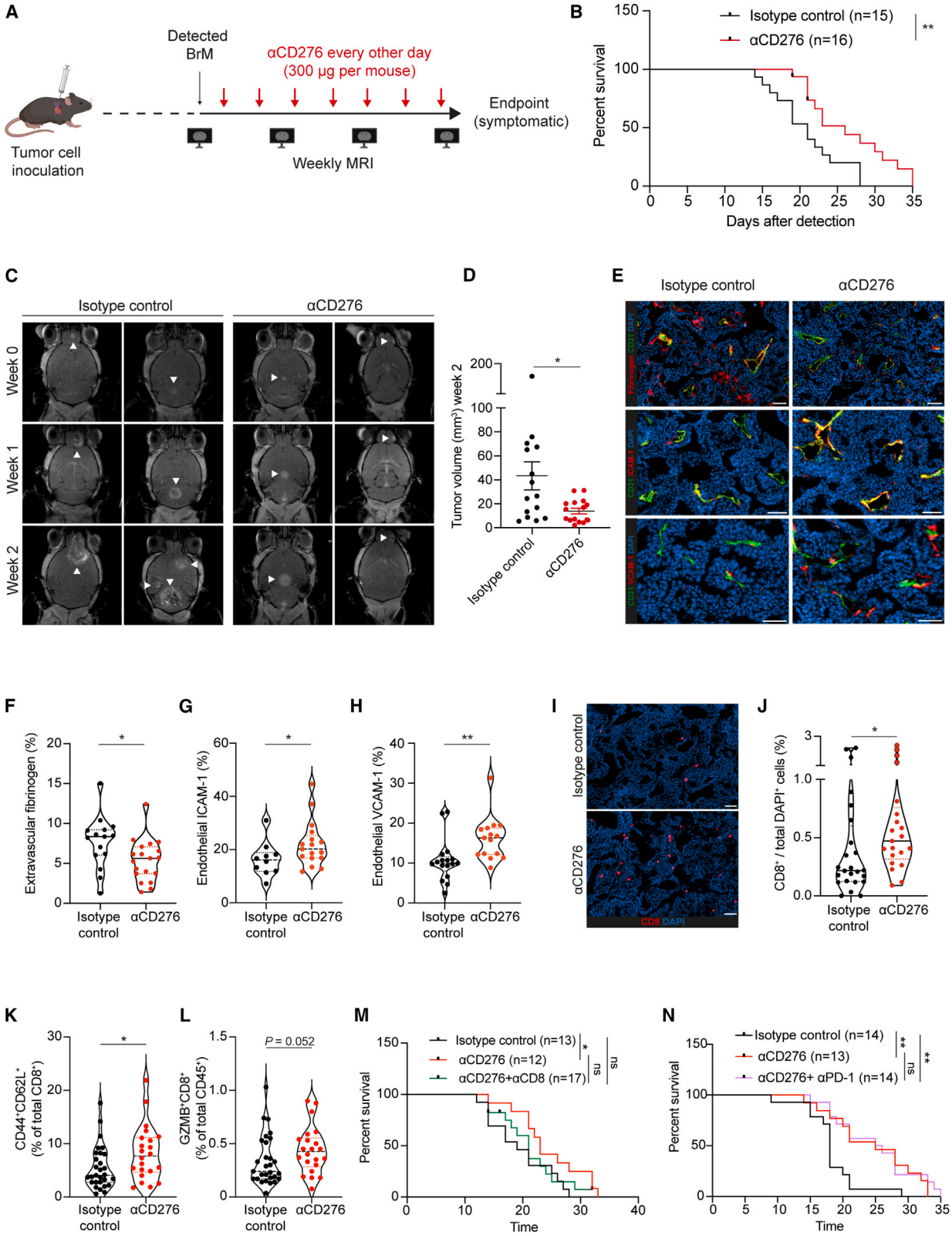

Figure 7. Evaluation of CD276-blocking antibodies in mouse breast to brain metastasis model

(A) Experimental design for BrM tumor induction, MRI monitoring, and mouse treatments.

(B) Kaplan-Meier survival curves of mice treated with αCD276 (n = 16) or isotype control (n = 15).

(legend continued on next page)

Recent advances have revealed the extensive heterogeneity of vascular components in multiple organs and pathological conditions.[30,56,57] Our study presents a comprehensive analysis of the major brain vascular components, endothelial cells and mural cells, in human BrM. Through scRNA-seq analyses, we revealed several EC subtypes independent of the arterio-venous axis, including those with "*angiogenic*", "*interferon*", and "*proliferative*" signatures. We also identified multiple mural cell subtypes, including "*transport*"-, "*interferon*"-, "*proliferative*",- and "*ECM*"-pericytes, SMCs, and fibroblasts. "*ECM*" and "*interferon*" pericytes represented the main populations in BrM samples, while non-tumor samples were enriched in "*transport*" pericytes and SMCs. Consistent with our findings, other studies also report the expression of transporters including *ATP1A2* and *SLC6A1* in human brain mural cells.[58]

Transcriptomic analyses comparing BrM vs. non-tumor endothelial and mural cells revealed a significantly altered vasculature characterized by increased ECM production and modification; compromised transporting systems and cell adhesion and junction molecules; proliferative and dysfunctional cell types with decreased capacity to maintain BBB homeostasis; and increased interactions with certain immune cells. Some of these findings, such as the upregulation of angiogenesis mediators or ECM molecules are consistent with analysis of lung-BrM ECs.[59] Interestingly, upon integration with primary tumor datasets,[41–44] we found that ECs in both breast- and lung-BrM, and mural cells in lung-BrM, are transcriptionally similar to those in GBM, indicating an instructive role of the brain environment in altering these cell phenotypes. By contrast, ECs and mural cells from melanoma-BrMs were more similar to their primary counterparts. It will be critical to now explore functionally whether these features can predict response to TME-targeted therapies in BrM. For example, the fact that melanoma-BrMs have a higher lymphocyte infiltration[8] and similar vascular properties to primary melanomas could be an indication of the better response of these patients to immunotherapies.

Importantly, our analysis of a panel of mouse BrM models recapitulated the vascular changes in human BrM, underscoring their value for exploring new therapeutic strategies directed to the tumor vasculature. Additionally, our results indicate that the aberrant BBB has an important role in shaping the BrM TME, as specific phenotypic signatures (e.g., BBB dysfunction or interferon scores) in endothelial and mural cells correlated with immune cell composition. By investigating the role of vascular components as key immune-regulatory players, we revealed enhanced expression of multiple immune checkpoint molecules and T cell apoptosis drivers. As proof-of-concept, we focused on the immune checkpoint molecule CD276, which was upregulated in both human and mouse endothelial and mural cells. CD276 is an immunosuppressive B7 family member (B7-H3) that inhibits T cell proliferation and promotes immune evasion by tumor cells, and high expression correlates with poor prognosis in several cancers.[51,60] CD276-targeting strategies have shown efficacy in preclinical models of extracranial cancers, and are currently being evaluated in clinical trials.[61] We now show that CD276 inhibition in a preclinical breast-BrM model significantly decreased metastatic growth and increased survival, indicating that targeting CD276 might also be a promising therapy for brain malignancies.

Given the anti-CD276 effect, it was logical to combine with PD-1 inhibition. However, there was no further enhancement of CD276 blockade, consistent with a profound immune-suppressive effect in the brain. This correlates with several clinical trials assessing ICB in BrM that only found an intracranial response in a small subgroup of patients with melanoma or lung cancer.[25,26] Future studies must address the challenge of brain immunosuppression from diverse perspectives, including detailed analyses of cytotoxic T cell specificity, activation, recruitment, and suppression by different brain TME components. From the vascular perspective, our study identifies additional immune inhibitory molecules enriched specifically in endothelial or mural cells (e.g., *CD200*, *LGALS9*, and *TDO2*) which, together with the downregulation of cell adhesion molecules that favor immune cell infiltration (e.g., *ICAM1*, *ICAM2*, or *VCAM1*) may explain, in part, the immune evasion in BrM. Therapeutically modulating these targets represents a promising strategy to overcome immune suppression.

In summary, this study reports a multifaceted interrogation of the key BrM vascular components which, together with the data generated in parallel from diverse mouse brain metastatic models, represents a valuable platform to interrogate novel vascular targets for the treatment of brain metastatic tumors.

Limitations of the study

A technical limitation is the large amount of material needed to obtain high-quality data for human scRNA-seq analyses. Since the surgical samples are variable in size, there were a smaller number of samples processed for scRNA-seq compared to our other analyses, and consequently, the patient heterogeneity may not be fully captured. Additionally, we isolated and sorted mural cells based on PDGFRβ expression, which is the broadest cell surface marker used to identify mural cells, being expressed by pericytes, smooth muscle cells, and fibroblasts, to varying degrees. However, some populations with low PDGFRβ expression levels, such as fibroblasts, may consequently be underrepresented in our study. It is important to note that in the bulk and scRNA-seq analyses, we used tissue from patients with epilepsy as non-tumor brain controls. These patients are younger than the

(C and D) Representative MRI images (C) and tumor volume quantification (D), 2 weeks after treatment with αCD276 (n = 16) or isotype control (n = 15). Data represented as mean ± SEM. Each dot represents a mouse.
(E–H) Representative IF images (E) and violin plot representation of (F) extravascular fibrinogen ($n_{Isotype}$ = 15, $n_{\alpha CD276}$ = 19), (G) endothelial ICAM-1 ($n_{Isotype}$ = 10, $n_{\alpha CD276}$ = 17), and (H) endothelial VCAM-1 ($n_{Isotype}$ = 17, $n_{\alpha CD276}$ = 15). Scale bar (E): 50 μm.
(I and J) Representative IF images (I) and violin plot representation (J) of double-positive $CD3^+CD8^+$ cells ($n_{Isotype}$ = 24, $n_{\alpha CD276}$ = 21). Scale bar (I): 50 μm.
(K and L) Violin plot representation of percentage of (K) central memory ($CD44^+CD62L^+$) $CD8^+$ T cells and (L) $GZMB^+CD8^+$ T cells in isotype control (n = 29) or αCD276 (n = 22) treatment groups.
(M) Kaplan-Meier survival curves of mice treated with isotype control (n = 13), αCD276 (n = 12), or αCD276 + αCD8 (n = 17).
(N) Kaplan-Meier survival curves of mice treated with isotype control (n = 14), αCD276 (n = 13), or αCD276 + αPD-1 (n = 14). Mantel-Cox test used in (B), (M), and (N). Each dot represents an individual metastasis in (F)–(H) and (J)–(L). Mann-Whitney two-tail test used in (D), (G), (H), (J), (K), and (L). Unpaired two-tail test used in (F). p values in panels (B), (D), (F–H), (J), and (K–N): *p < 0.05, **p < 0.01, ***p < 0.001, ns = non-significant. Also see Figure S7.

average age of patients with BrM in our cohort, so we cannot exclude aging-associated transcriptional changes among the alterations identified in endothelial and mural cells. Finally, the human and murine brain tumors analyzed represented late-stage tumors, and both endothelial and mural cells may differ at early stages of BrM formation. However, examining the initial steps of cancer cell extravasation in patients is technically challenging due to brain tissue access. Based on the high conservation between human and mouse vascular alterations revealed herein, for future studies it will be instructive to employ mouse models and advanced techniques, including spatial transcriptomics, to fully unravel the complex changes in the tumor vasculature over the dynamic course of BrM development and progression.

STAR★METHODS

Detailed methods are provided in the online version of this paper and include the following:

- KEY RESOURCES TABLE
- RESOURCE AVAILABILITY
  - Lead contact
  - Materials availability
  - Data and code availability
- EXPERIMENTAL MODEL AND STUDY PARTICIPANT DETAILS
  - Human subjects
  - Mouse models
  - Cell lines
- METHOD DETAILS
  - Endothelial cell and mural cell isolation using fluorescence-activated cell sorting
  - Single-cell RNA-sequencing
  - Bulk RNA-sequencing
  - Immunofluorescence staining
  - Image analysis
  - Generation of experimental brain metastasis
  - Mouse monitoring by magnetic resonance imaging (MRI)
  - Measuring blood-brain barrier leakage using gadolinium enhanced MRI
  - Mouse treatments
  - Flow cytometry analysis of T cell phenotype
  - Statistical analysis

SUPPLEMENTAL INFORMATION

Supplemental information can be found online at https://doi.org/10.1016/j.ccell.2023.12.018.

ACKNOWLEDGMENTS

We are very grateful to all patients who generously donated tissue for this study. We express our gratitude to the Departments of Neurosurgery, Neuro-oncology, and Pathology at CHUV Lausanne; Dr. Benoit Duc; members of Prof. Hegi's lab; and Prof. Ron Stoop for their support in coordinating, obtaining, processing, and annotating patient tissue collection. We thank all Joyce lab members for stimulating scientific discussions; Dr. Jeremiah Bernier-Latmani for vascular biology insights; Dr. Pratyaksha Wirapati for bioinformatic support; and the mouse pathology, animal facilities and flow cytometry Core Facilities of UNIL for technical support and advice. We thank Profs. Michele de Palma and Etienne Meylan for generously sharing the parental KP mouse lung cancer cell line, and Alan Guichard for technical advice. This research was supported in part by the Swiss National Science Foundation Advanced Grant TMAG-3_209224, Ludwig Institute for Cancer Research, University of Lausanne, Carigest Foundation, Breast Cancer Research Foundation, and Lundin Brain Tumor Center (to J.A.J.). L.B. gratefully acknowledges postdoctoral fellowships from European Molecular Biology Organisation (ALTF 1193-2018) and Human Frontier Science Program (LT000038/2019). M.M. was supported in part by AIRC and European Union's Horizon 2020 research and innovation program (800924).

AUTHOR CONTRIBUTIONS

L.B. and J.A.J. conceived the study, designed experiments, and interpreted data. L.B. processed all clinical samples. L.B. performed the majority of experiments and analyses with support from E.L. and M.B. A.K., N.F., and J.L. performed RNA-seq analyses. L.B. and R.C. performed MRI analysis. M.M., K.S., and J.L. generated the murine lung brain-homing cell line. A.F.H., R.T.D., and M.E.H. provided clinical material. R.M., S.G., and K.S. aided with coordination, banking and annotation of clinical material. J-P.B. provided histopathological reviews. L.B. prepared the figures. L.B. and J.A.J. wrote the manuscript. J.A.J. supervised the study. All authors reviewed, edited, or commented on the manuscript.

DECLARATION OF INTERESTS

M.E.H. has an advisory role at TME Pharma.

Received: April 3, 2023
Revised: October 11, 2023
Accepted: December 20, 2023
Published: January 18, 2024

REFERENCES

1. Eichler, A.F., Chung, E., Kodack, D.P., Loeffler, J.S., Fukumura, D., and Jain, R.K. (2011). The biology of brain metastases-translation to new therapies. Nat. Rev. Clin. Oncol. *8*, 344–356.
2. Valiente, M., Ahluwalia, M.S., Boire, A., Brastianos, P.K., Goldberg, S.B., Lee, E.Q., Le Rhun, E., Preusser, M., Winkler, F., and Soffietti, R. (2018). The Evolving Landscape of Brain Metastasis. Trends Cancer *4*, 176–196.
3. Suh, J.H., Kotecha, R., Chao, S.T., Ahluwalia, M.S., Sahgal, A., and Chang, E.L. (2020). Current approaches to the management of brain metastases. Nat. Rev. Clin. Oncol. *17*, 279–299.
4. Steindl, A., Brunner, T.J., Heimbach, K., Schweighart, K., Moser, G.M., Niziolek, H.M., Moor, E., Kreminger, J., Starzer, A.M., Dieckmann, K., et al. (2022). Changing characteristics, treatment approaches and survival of patients with brain metastasis: data from six thousand and thirty-one individuals over an observation period of 30 years. Eur. J. Cancer *162*, 170–181.
5. Quail, D.F., and Joyce, J.A. (2017). The Microenvironmental Landscape of Brain Tumors. Cancer Cell *31*, 326–341.
6. de Visser, K.E., and Joyce, J.A. (2023). The evolving tumor microenvironment: From cancer initiation to metastatic outgrowth. Cancer Cell *41*, 374–403.
7. Friebel, E., Kapolou, K., Unger, S., Núñez, N.G., Utz, S., Rushing, E.J., Regli, L., Weller, M., Greter, M., Tugues, S., et al. (2020). Single-Cell Mapping of Human Brain Cancer Reveals Tumor-Specific Instruction of Tissue-Invading Leukocytes. Cell *181*, 1626–1642.e20.
8. Klemm, F., Maas, R.R., Bowman, R.L., Kornete, M., Soukup, K., Nassiri, S., Brouland, J.P., Iacobuzio-Donahue, C.A., Brennan, C., Tabar, V., et al. (2020). Interrogation of the Microenvironmental Landscape in Brain Tumors Reveals Disease-Specific Alterations of Immune Cells. Cell *181*, 1643–1660.e17.
9. Gonzalez, H., Mei, W., Robles, I., Hagerling, C., Allen, B.M., Hauge Okholm, T.L., Nanjaraj, A., Verbeek, T., Kalavacherla, S., van Gogh, M., et al. (2022). Cellular architecture of human brain metastases. Cell *185*, 729–745.e20.

10. Karimi, E., Yu, M.W., Maritan, S.M., Perus, L.J.M., Rezanejad, M., Sorin, M., Dankner, M., Fallah, P., Doré, S., Zuo, D., et al. (2023). Single-cell spatial immune landscapes of primary and metastatic brain tumours. Nature *614*, 555–563.

11. Wischnewski, V., Maas, R.R., Aruffo, P.G., Soukup, K., Galletti, G., Kornete, M., Galland, S., Fournier, N., Lilja, J., Wirapati, P., et al. (2023). Phenotypic diversity of T cells in human primary and metastatic brain tumors revealed by multiomic interrogation. Nat. Cancer *4*, 908–924.

12. Maas, R.R., Soukup, K., Fournier, N., Massara, M., Galland, S., Kornete, M., Wischnewski, V., Lourenco, J., Croci, D., Álvarez-Prado, Á.F., et al. (2023). The local microenvironment drives activation of neutrophils in human brain tumors. Cell *186*, 4546–4566.e27.

13. Álvarez-Prado, Á.F., Maas, R.R., Soukup, K., Klemm, F., Kornete, M., Krebs, F.S., Zoete, V., Berezowska, S., Brouland, J.-P., Hottinger, A.F., et al. (2023). Immunogenomic analysis of human brain metastases reveals diverse immune landscapes across genetically distinct tumors. Cell Rep. Med. *4*, 100900.

14. Wilhelm, I., Molnar, J., Fazakas, C., Hasko, J., and Krizbai, I.A. (2013). Role of the blood-brain barrier in the formation of brain metastases. Int. J. Mol. Sci. *14*, 1383–1411.

15. Fares, J., Kanojia, D., Rashidi, A., Ulasov, I., and Lesniak, M.S. (2020). Genes that Mediate Metastasis across the Blood–Brain Barrier. Trends Cancer *6*, 660–676.

16. Bos, P.D., Zhang, X.H.F., Nadal, C., Shu, W., Gomis, R.R., Nguyen, D.X., Minn, A.J., Van De Vijver, M.J., Gerald, W.L., Foekens, J.A., and Massagué, J. (2009). Genes that mediate breast cancer metastasis to the brain. Nature *459*, 1005–1009.

17. Sevenich, L., Bowman, R.L., Mason, S.D., Quail, D.F., Rapaport, F., Elie, B.T., Brogi, E., Brastianos, P.K., Hahn, W.C., Holsinger, L.J., et al. (2014). Analysis of tumour- and stroma-supplied proteolytic networks reveals a brain-metastasis-promoting role for cathepsin S. Nat. Cell Biol. *16*, 876–888.

18. Jilaveanu, L.B., Parisi, F., Barr, M.L., Zito, C.R., Cruz-Munoz, W., Kerbel, R.S., Rimm, D.L., Bosenberg, M.W., Halaban, R., Kluger, Y., and Kluger, H.M. (2015). PLEKHA5 as a biomarker and potential mediator of melanoma brain metastasis. Clin. Cancer Res. *21*, 2138–2147.

19. Li, B., Wang, C., Zhang, Y., Zhao, X.Y., Huang, B., Wu, P.F., Li, Q., Li, H., Liu, Y.S., Cao, L.Y., et al. (2013). Elevated PLGF contributes to small-cell lung cancer brain metastasis. Oncogene *32*, 2952–2962.

20. Doron, H., Amer, M., Ershaid, N., Blazquez, R., Shani, O., Lahav, T.G., Cohen, N., Adler, O., Hakim, Z., Pozzi, S., et al. (2019). Inflammatory Activation of Astrocytes Facilitates Melanoma Brain Tropism via the CXCL10-CXCR3 Signaling Axis. Cell Rep. *28*, 1785–1798.e6.

21. Adler, O., Zait, Y., Cohen, N., Blazquez, R., Doron, H., Monteran, L., Scharff, Y., Shami, T., Mundhe, D., Glehr, G., et al. (2023). Reciprocal interactions between innate immune cells and astrocytes facilitate neuroinflammation and brain metastasis via lipocalin-2. Nat. Cancer *4*, 401–418.

22. Valiente, M., Obenauf, A.C., Jin, X., Chen, Q., Zhang, X.H.-F., Lee, D.J., Chaft, J.E., Kris, M.G., Huse, J.T., Brogi, E., and Massagué, J. (2014). Serpins Promote Cancer Cell Survival and Vascular Co-Option in Brain Metastasis. Cell *156*, 1002–1016.

23. Er, E.E., Valiente, M., Ganesh, K., Zou, Y., Agrawal, S., Hu, J., Griscom, B., Rosenblum, M., Boire, A., Brogi, E., et al. (2018). Pericyte-like spreading by disseminated cancer cells activates YAP and MRTF for metastatic colonization. Nat. Cell Biol. *20*, 966–978.

24. Blecharz, K.G., Colla, R., Rohde, V., and Vajkoczy, P. (2015). Control of the blood-brain barrier function in cancer cell metastasis. Biol. Cell *107*, 342–371.

25. Goldberg, S.B., Schalper, K.A., Gettinger, S.N., Mahajan, A., Herbst, R.S., Chiang, A.C., Lilenbaum, R., Wilson, F.H., Omay, S.B., Yu, J.B., et al. (2020). Pembrolizumab for management of patients with NSCLC and brain metastases: long-term results and biomarker analysis from a non-randomised, open-label, phase 2 trial. Lancet Oncol. *21*, 655–663.

26. Tawbi, H.A., Forsyth, P.A., Hodi, F.S., Algazi, A.P., Hamid, O., Lao, C.D., Moschos, S.J., Atkins, M.B., Lewis, K., Postow, M.A., et al. (2021). Long-term outcomes of patients with active melanoma brain metastases treated with combination nivolumab plus ipilimumab (CheckMate 204): final results of an open-label, multicentre, phase 2 study. Lancet Oncol. *22*, 1692–1704.

27. Amersfoort, J., Eelen, G., and Carmeliet, P. (2022). Immunomodulation by endothelial cells — partnering up with the immune system? Nat. Rev. Immunol. *22*, 576–588.

28. Winkler, E.A., Kim, C.N., Ross, J.M., Garcia, J.H., Gil, E., Oh, I., Chen, L.Q., Wu, D., Catapano, J.S., Raygor, K., et al. (2022). A single-cell atlas of the normal and malformed human brain vasculature. Science *375*, eabi7377.

29. Vanlandewijck, M., He, L., Mäe, M.A., Andrae, J., Ando, K., Del Gaudio, F., Nahar, K., Lebouvier, T., Laviña, B., Gouveia, L., et al. (2018). A molecular atlas of cell types and zonation in the brain vasculature. Nature *554*, 475–480.

30. Wälchli, T., Bisschop, J., Carmeliet, P., Zadeh, G., Monnier, P.P., De Bock, K., and Radovanovic, I. (2023). Shaping the brain vasculature in development and disease in the single-cell era. Nat. Rev. Neurosci. *24*, 1–28.

31. Garcia, F.J., Sun, N., Lee, H., Godlewski, B., Mathys, H., Galani, K., Zhou, B., Jiang, X., Ng, A.P., Mantero, J., et al. (2022). Single-cell dissection of the human brain vasculature. Nature *603*, 893–899.

32. Yang, A.C., Vest, R.T., Kern, F., Lee, D.P., Agam, M., Maat, C.A., Losada, P.M., Chen, M.B., Schaum, N., Khoury, N., et al. (2022). A human brain vascular atlas reveals diverse mediators of Alzheimer's risk. Nature *603*, 885–892.

33. Trimm, E., and Red-Horse, K. (2023). Vascular endothelial cell development and diversity. Nat. Rev. Cardiol. *20*, 197–210.

34. Bosma, E.K., van Noorden, C.J.F., Schlingemann, R.O., and Klaassen, I. (2018). The role of plasmalemma vesicle-associated protein in pathological breakdown of blood–brain and blood–retinal barriers: potential novel therapeutic target for cerebral edema and diabetic macular edema. Fluids Barriers CNS *15*, 24.

35. Kiselev, V.Y., Yiu, A., and Hemberg, M. (2018). scmap: projection of single-cell RNA-seq data across data sets. Nat. Methods *15*, 359–362.

36. Geldhof, V., de Rooij, L.P.M.H., Sokol, L., Amersfoort, J., De Schepper, M., Rohlenova, K., Hoste, G., Vanderstichele, A., Delsupehe, A.-M., Isnaldi, E., et al. (2022). Single cell atlas identifies lipid-processing and immunomodulatory endothelial cells in healthy and malignant breast. Nat. Commun. *13*, 5511.

37. Goveia, J., Rohlenova, K., Taverna, F., Treps, L., Conradi, L.-C., Pircher, A., Geldhof, V., de Rooij, L.P.M.H., Kalucka, J., Sokol, L., et al. (2020). An Integrated Gene Expression Landscape Profiling Approach to Identify Lung Tumor Endothelial Cell Heterogeneity and Angiogenic Candidates. Cancer Cell *37*, 21–36.e13.

38. Ochs, K., Sahm, F., Opitz, C.A., Lanz, T.V., Oezen, I., Couraud, P.-O., von Deimling, A., Wick, W., and Platten, M. (2013). Immature mesenchymal stem cell-like pericytes as mediators of immunosuppression in human malignant glioma. J. Neuroimmunol. *265*, 106–116.

39. Munji, R.N., Soung, A.L., Weiner, G.A., Sohet, F., Semple, B.D., Trivedi, A., Gimlin, K., Kotoda, M., Korai, M., Aydin, S., et al. (2019). Profiling the mouse brain endothelial transcriptome in health and disease models reveals a core blood–brain barrier dysfunction module. Nat. Neurosci. *22*, 1892–1902.

40. Hariharan, A., Weir, N., Robertson, C., He, L., Betsholtz, C., and Longden, T.A. (2020). The Ion Channel and GPCR Toolkit of Brain Capillary Pericytes. Front. Cell. Neurosci. *14*, 601324.

41. Wu, S.Z., Al-Eryani, G., Roden, D.L., Junankar, S., Harvey, K., Andersson, A., Thennavan, A., Wang, C., Torpy, J.R., Bartonicek, N., et al. (2021). A single-cell and spatially resolved atlas of human breast cancers. Nat. Genet. *53*, 1334–1347.

42. Salcher, S., Sturm, G., Horvath, L., Untergasser, G., Kuempers, C., Fotakis, G., Panizzolo, E., Martowicz, A., Trebo, M., Pall, G., et al. (2022). High-resolution single-cell atlas reveals diversity and plasticity of tissue-resident neutrophils in non-small cell lung cancer. Cancer Cell *40*, 1503–1520.e8.

43. Jerby-Arnon, L., Shah, P., Cuoco, M.S., Rodman, C., Su, M.-J., Melms, J.C., Leeson, R., Kanodia, A., Mei, S., Lin, J.-R., et al. (2018). A Cancer

Cell Program Promotes T Cell Exclusion and Resistance to Checkpoint Blockade. Cell *175*, 984–997.e24.

44. Abdelfattah, N., Kumar, P., Wang, C., Leu, J.-S., Flynn, W.F., Gao, R., Baskin, D.S., Pichumani, K., Ijare, O.B., Wood, S.L., et al. (2022). Single-cell analysis of human glioma and immune cells identifies S100A4 as an immunotherapy target. Nat. Commun. *13*, 767.
45. Cuervo, H., Pereira, B., Nadeem, T., Lin, M., Lee, F., Kitajewski, J., and Lin, C.-S. (2017). PDGFRβ-P2A-CreERT2 mice: a genetic tool to target pericytes in angiogenesis. Angiogenesis *20*, 655–662.
46. Török, O., Schreiner, B., Schaffenrath, J., Tsai, H.-C., Maheshwari, U., Stifter, S.A., Welsh, C., Amorim, A., Sridhar, S., Utz, S.G., et al. (2021). Pericytes regulate vascular immune homeostasis in the CNS. Proc. Natl. Acad. Sci. USA *118*, e2016587118.
47. McLarnon, J.G. (2021). A Leaky Blood–Brain Barrier to Fibrinogen Contributes to Oxidative Damage in Alzheimer's Disease. Antioxidants *11*, 102.
48. Cooke, V.G., LeBleu, V.S., Keskin, D., Khan, Z., O'Connell, J.T., Teng, Y., Duncan, M.B., Xie, L., Maeda, G., Vong, S., et al. (2012). Pericyte Depletion Results in Hypoxia-Associated Epithelial-to-Mesenchymal Transition and Metastasis Mediated by Met Signaling Pathway. Cancer Cell *21*, 66–81.
49. Ku, M.-C., Waiczies, S., Niendorf, T., and Pohlmann, A. (2018). In Assessment of Blood Brain Barrier Leakage with Gadolinium-Enhanced MRI. In Preclinical MRI. Methods in Molecular Biology. García Martín, López Larrubia P., ed. (Humana Press), pp. 395–408.
50. Chen, J., Luo, Y., Hui, H., Cai, T., Huang, H., Yang, F., Feng, J., Zhang, J., and Yan, X. (2017). CD146 coordinates brain endothelial cell–pericyte communication for blood–brain barrier development. Proc. Natl. Acad. Sci. USA *114*, E7622–E7631.
51. Zhao, B., Li, H., Xia, Y., Wang, Y., Wang, Y., Shi, Y., Xing, H., Qu, T., Wang, Y., and Ma, W. (2022). Immune checkpoint of B7-H3 in cancer: from immunology to clinical immunotherapy. J. Hematol. Oncol. *15*, 153.
52. Wang, C., Li, Y., Jia, L., Kim, J.K., Li, J., Deng, P., Zhang, W., Krebsbach, P.H., and Wang, C.-Y. (2021). CD276 expression enables squamous cell carcinoma stem cells to evade immune surveillance. Cell Stem Cell *28*, 1597–1613.e7.
53. Yonesaka, K., Haratani, K., Takamura, S., Sakai, H., Kato, R., Takegawa, N., Takahama, T., Tanaka, K., Hayashi, H., Takeda, M., et al. (2018). B7-H3 Negatively Modulates CTL-Mediated Cancer Immunity. Clin. Cancer Res. *24*, 2653–2664.
54. Yamato, I., Sho, M., Nomi, T., Akahori, T., Shimada, K., Hotta, K., Kanehiro, H., Konishi, N., Yagita, H., and Nakajima, Y. (2009). Clinical importance of B7-H3 expression in human pancreatic cancer. Br. J. Cancer *101*, 1709–1716.
55. Steeg, P.S. (2021). The blood–tumour barrier in cancer biology and therapy. Nat. Rev. Clin. Oncol. *18*, 696–714.
56. Chavkin, N.W., and Hirschi, K.K. (2020). Single Cell Analysis in Vascular Biology. Front. Cardiovasc. Med. *7*, 42.
57. Crouch, E.E., and Doetsch, F. (2018). FACS isolation of endothelial cells and pericytes from mouse brain microregions. Nat. Protoc. *13*, 738–751.
58. Gastfriend, B.D., Foreman, K.L., Katt, M.E., Palecek, S.P., and Shusta, E.V. (2021). Integrative analysis of the human brain mural cell transcriptome. J. Cereb. Blood Flow Metab. *41*, 3052–3068.
59. Schaffenrath, J., Wyss, T., He, L., Rushing, E.J., Delorenzi, M., Vasella, F., Regli, L., Neidert, M.C., and Keller, A. (2021). Blood-brain barrier alterations in human brain tumors revealed by genome-wide transcriptomic profiling. Neuro Oncol. *23*, 2095–2106.
60. Dai, L., Guo, X., Xing, Z., Tao, Y., Liang, W., Shi, Z., Hu, W., Zhou, S., and Wang, X. (2023). Multi-omics analyses of CD276 in pan-cancer reveals its clinical prognostic value in glioblastoma and other major cancer types. BMC Cancer *23*, 102.
61. Zhou, W.-T., and Jin, W.-L. (2021). B7-H3/CD276: An Emerging Cancer Immunotherapy. Front. Immunol. *12*, 701006.
62. Croci, D., Santalla Méndez, R., Temme, S., Soukup, K., Fournier, N., Zomer, A., Colotti, R., Wischnewski, V., Flögel, U., van Heeswijk, R.B., and Joyce, J.A. (2022). Multispectral fluorine-19 MRI enables longitudinal and noninvasive monitoring of tumor-associated macrophages. Sci. Transl. Med. *14*, eabo2952.
63. Saltarin, F., Wegmüller, A., Bejarano, L., Ildiz, E.S., Zwicky, P., Vianin, A., Spadin, F., Soukup, K., Wischnewski, V., Engelhardt, B., et al. (2023). Compromised Blood-Brain Barrier Junctions Enhance Melanoma Cell Intercalation and Extravasation. Cancers *15*, 5071.
64. Bankhead, P., Loughrey, M.B., Fernández, J.A., Dombrowski, Y., McArt, D.G., Dunne, P.D., McQuaid, S., Gray, R.T., Murray, L.J., Coleman, H.G., et al. (2017). QuPath: Open source software for digital pathology image analysis. Sci. Rep. *7*, 16878.
65. Dobin, A., Davis, C.A., Schlesinger, F., Drenkow, J., Zaleski, C., Jha, S., Batut, P., Chaisson, M., and Gingeras, T.R. (2013). STAR: ultrafast universal RNA-seq aligner. Bioinformatics *29*, 15–21.
66. Li, B., and Dewey, C.N. (2011). RSEM: accurate transcript quantification from RNA-Seq data with or without a reference genome. BMC Bioinf. *12*, 323.
67. Hao, Y., Hao, S., Andersen-Nissen, E., Mauck, W.M., Zheng, S., Butler, A., Lee, M.J., Wilk, A.J., Darby, C., Zager, M., et al. (2021). Integrated analysis of multimodal single-cell data. Cell *184*, 3573–3587.e29.
68. Andreatta, M., and Carmona, S.J. (2021). STACAS: Sub-Type Anchor Correction for Alignment in Seurat to integrate single-cell RNA-seq data. Bioinformatics *37*, 882–884.
69. Madisen, L., Zwingman, T.A., Sunkin, S.M., Oh, S.W., Zariwala, H.A., Gu, H., Ng, L.L., Palmiter, R.D., Hawrylycz, M.J., Jones, A.R., et al. (2010). A robust and high-throughput Cre reporting and characterization system for the whole mouse brain. Nat. Neurosci. *13*, 133–140.
70. Meeth, K., Wang, J.X., Micevic, G., Damsky, W., and Bosenberg, M.W. (2016). The YUMM lines: a series of congenic mouse melanoma cell lines with defined genetic alterations. Pigment Cell Melanoma Res. *29*, 590–597.
71. Gros, L., Ursino, C., Constanzo, J., Zangger, N., Meylan, E., Bonnefoy, N., and Faget, J. (2021). Low STING expression in a transplantable KrasG12D/P53ko lung cancer model contributes to SiglecF+ neutrophil and CD103+Treg accumulation in tumors. Preprint at bioRxiv. https://doi.org/10.1101/2021.01.04.425311.
72. Dorrier, C.E., Jones, H.E., Pintarić, L., Siegenthaler, J.A., and Daneman, R. (2022). Emerging roles for CNS fibroblasts in health, injury and disease. Nat. Rev. Neurosci. *23*, 23–34.
73. Wu, T., Hu, E., Xu, S., Chen, M., Guo, P., Dai, Z., Feng, T., Zhou, L., Tang, W., Zhan, L., et al. (2021). clusterProfiler 4.0: A universal enrichment tool for interpreting omics data. Innovation *2*, 100141.
74. Bennett, D.A., Buchman, A.S., Boyle, P.A., Barnes, L.L., Wilson, R.S., and Schneider, J.A. (2018). Religious Orders Study and Rush Memory and Aging Project. J. Alzheimer's Dis. *64*, S161–S189.
75. Robinson, M.D., McCarthy, D.J., and Smyth, G.K. (2010). edgeR: a Bioconductor package for differential expression analysis of digital gene expression data. Bioinformatics *26*, 139–140.
76. Ritchie, M.E., Phipson, B., Wu, D., Hu, Y., Law, C.W., Shi, W., and Smyth, G.K. (2015). limma powers differential expression analyses for RNA-sequencing and microarray studies. Nucleic Acids Res. *43*, e47.
77. Leek, J.T., Johnson, W.E., Parker, H.S., Fertig, E.J., Jaffe, A.E., Zhang, Y., Storey, J.D., and Torres, L.C. (2021). Surrogate Variable Analysis. R Package Version 3.42.0.
78. Schmidt, U., Weigert, M., and Broaddus, C. (2018). Myers G. Cell Detection with Star-Convex Polygons. In In Medical Image Computing and Computer Assisted Intervention – MICCAI., A. Frangi, J. Schnabel, C. Davatzikos, C. Alberola-López, and G. Fichtinger, eds. (Springer, Cham: Lecture Notes in Computer Science), pp. 265–273.

STAR★METHODS

KEY RESOURCES TABLE

REAGENT or RESOURCE	SOURCE	IDENTIFIER
Antibodies		
IF: anti-mouse CD31 (goat polyclonal)	RD Systems	Cat# AF3628; RRID: AB_2161028
IF: anti-mouse CD31 (rat monoclonal ER-MP12)	Bio-Rad	Cat# MCA2388GA; RRID: AB_2161024
IF: anti-human CD31 (sheep polyclonal)	RD Systems	Cat# AF806; RRID: AB_355617
IF: anti-human CD31 (mouse monoclonal JC/70A)	Invitrogen	Cat# MA5-13188; RRID: AB_10982120
IF: anti human/mouse PDGFRβ (rabbit monoclonal Y92)	Abcam	Cat# ab32570; RRID: AB_777165
IF/FCM: anti-human PDGFRβ/CD140b-PE (mouse monoclonal 28D4)	BD	Cat# 558821; RRID: AB_397132
IF: anti-human/mouse Fibrinogen (rabbit polyclonal)	Agilent Technologies	Cat# A008002-2; RRID: AB_578481
IF: anti-mouse CD45-PE (rat monoclonal 30-F11)	BioLegend	Cat# 103106; RRID: AB_312971
IF: anti-mouse CD45-FITC (rat monoclonal 30-F11)	BD	Cat# 553080; RRID: AB_394610
IF: anti-human CD45-AF488 (mouse monoclonal HI30)	BioLegend	Cat# 304017; RRID: AB_389314
IF: anti-mouse Iba-1 (rabbit polyclonal)	Wako	Cat# 019-19741; RRID: AB_839504
IF: anti-mouse CD8a-AF647 (rat monoclonal 53-6.7)	BioLegend	Cat# 100724; RRID: AB_389326
IF: anti-mouse CD3-AF750 (rat monoclonal 17A2)	RD Systems	Cat# FAB4841S-025; RRID: NA
IF: anti-human/mouse CD276 (rabbit monoclonal EPNCIR122)	Abcam	Cat# ab134161; RRID: AB_2687929
IF: anti-human/mouse CD200 (goat polyclonal)	RD Systems	Cat# AF2724; RRID: AB_416669
IF: anti-human/mouse Collagen-IV (goat polyclonal)	Bio-Rad	Cat# 134001; RRID: AB_2082646
IF: anti-human/mouse Ki-67-APC (rat monoclonal SolA15)	Invitrogen	Cat# 17-5698-82; RRID: AB_2688057
IF: anti-human/mouse IFIT1 (rabbit polyclonal)	Abcam	Cat# ab236256; RRID: NA
IF: anti-human ESM-1 (mouse monoclonal MEP08)	Biothelis	Cat# LIA-0901S; RRID: NA
IF: anti-human MYH11 (rabbit monoclonal EPR5336(B))	Abcam	Cat# ab133567; RRID: AB_2890982
IF: anti-mouse/human ER-TR7 (rat monoclonal ER-TR7)	Novus Biologicals	Cat# NB100-64932; RRID: AB_963381
IF: anti-human ALPL (rabbit polyclonal)	Atlas antibodies	Cat# HPA008765; RRID: AB_1078138
IF: anti-human ACKR1 (rabbit polyclonal)	Atlas antibodies	Cat# HPA016421; RRID: AB_1849219
IF: anti-human SLC16A1 (rabbit polyclonal)	OriGene	Cat# TA321556; RRID: NA
IF: anti-human GABA transporter-1, SLC6A1 (rabbit polyclonal)	Merk	Cat# AB1570; RRID: AB_11213673
IF: anti-human OLFML2B (rabbit polyclonal)	LSBio	Cat# LS-C356234; RRID: NA
IF: anti-human/mouse Claudin 5 (rabbit polyclonal)	Invitrogen	Cat# 34-1600; RRID: AB_2533157
IF: anti-mouse ICAM1-AF647 (rat monoclonal YN1/1.7.4)	BioLegend	CAT# 116113; RRID: AB_493496
IF: anti-mouse ICAM1 (Rat monoclonal YN1/1.7.4)	Abcam	Cat# ab119871; RRID: AB_10900211
IF: anti-mouse VCAM1 (goat polyclonal)	RD Systems	Cat# AF643; RRID: AB_355499
IF: anti-mouse/human MCAM/CD146 (rabbit monoclonal EPR3208)	Abcam	Cat# ab75769; RRID: AB_2143375
IF: anti-mouse CD62E-PE (rat monoclonal 10E9.6)	BD	Cat# 553751; RRID: AB_395031
IF: anti-mouse ICAM2/CD102 (rat monoclonal 3C4(mIC2/4))	BD	Cat# 553326; RRID: AB_394784
IF: AF647 anti-rabbit IgG (donkey polyclonal)	Invitrogen	Cat# A-31573; RRID: AB_2536183
IF: DyLight755 anti-goat IgG (donkey polyclonal)	Invitrogen	Cat# SA5-10091; RRID: AB_2556671
IF: AF488 anti-rat IgG (donkey polyclonal)	Invitrogen	Cat# A21208; RRID: AB_2535794
IF: AF647 anti-goat IgG (donkey polyclonal)	Invitrogen	Cat# A32849; RRID: AB_2762840
IF: AF488 anti-goat IgG (donkey polyclonal)	Invitrogen	Cat# A11055/A32814; RRID: AB_2534102/AB_2762838
IF: AF555 anti-rabbit IgG (donkey polyclonal)	Invitrogen	Cat# A31572; RRID: AB_162543
IF: DyLight755 anti-rabbit IgG (donkey polyclonal)	Invitrogen	Cat# SA5-10043; RRID: AB_2556623

(*Continued on next page*)

Continued

REAGENT or RESOURCE	SOURCE	IDENTIFIER
IF: AF750 anti-sheep IgG (donkey polyclonal)	Abcam	Cat# ab175756; RRID: NA
IF: AF647 anti-mouse IgG (donkey polyclonal)	Invitrogen	Cat# A31571; RRID: AB_162542
IF: AF488 anti-mouse IgG (donkey polyclonal)	Invitrogen	Cat# A32766; RRID: AB_2762823
IF: AF488 anti-sheep IgG (donkey polyclonal)	Invitrogen	Cat# A11015; RRID: AB_2534082
IF: DyLight755 anti-mouse IgG (donkey polyclonal)	Invitrogen	Cat# SA5-10171; RRID: AB_2556751
IF: DyLight755 anti-rat IgG (donkey polyclonal)	Invitrogen	Cat# SA5-10031; RRID: AB_2556611
IF: DyLight650 anti-rat IgG (donkey polyclonal)	Invitrogen	Cat# SA5-10029; RRID: AB_2556609
IF: AF488 anti-rabbit (donkey polyclonal)	Invitrogen	Cat# A21206; RRID: AB_2535792
IF: AF647 anti-rat IGg2a (mouse monoclonal MRG2a-83)	BioLegend	Cat# 407512; RRID: AB_2716140
IF: AF647 anti-rat IGg2b (mouse monoclonal 2B 10A8)	Abcam	Cat# ab172335; RRID: NA
IF: AF555 anti-goat IgG (donkey polyclonal)	Invitrogen	Cat# A21432; RRID: AB_2535853
IF: DAPI (4',6-Diamidino-2-Phenylindole, Dihydrochloride)	Invitrogen	Cat# D1306; RRID: AB_2629482
FCM: anti-mouse CD11b BUV661 (rat monoclonal M1/70)	BD	Cat# 612977; RRID: AB_2870249
FCM: anti-mouse CD45 AF700 (rat monoclonal 30-F11)	BioLegend	Cat# 103128; RRID: AB_493715
FCM: anti-mouse CD326 (Ep-CAM) BV421 (rat monoclonal G8.8)	BioLegend	Cat# 118225; RRID: AB_2563983
FCM: anti-mouse CD31 PE/Cy7 (rat monoclonal 390)	BioLegend	Cat# 102418; RRID: AB_830757
FCM: anti-human CD45 BV421 (mouse monoclonal HI30)	BioLegend	Cat# 304031; RRID: AB_10900423
FCM: anti-human CD11b BUV563 (rat monoclonal M1/70)	BD	Cat# 741242; RRID: AB_2870793
FCM: anti-human CD31 APC (mouse monoclonal WM59)	BioLegend	Cat# 303116; RRID: AB_1877151
FCM : anti-mouse CD45 BUV395 (rat monoclonal 30-F11)	BD	Cat# 564279; RRID: AB_2651134
FCM : anti-mouse TCRβ BV421 (armenian hamster monoclonal H57-597)	BioLegend	Cat# 109229; RRID: AB_10933263
FCM : anti-mouse CD8a BV711 (rat monoclonal 53-6.7)	BioLegend	Cat# 100759; RRID: AB_2563510
FCM : anti-mouse CD62L BV785 (rat monoclonal MEL-14)	BioLegend	Cat# 104440; RRID: AB_2629685
FCM : anti-mouse CD44 BV510 (rat monoclonal IM7)	BioLegend	Cat# 103043; RRID: AB_2561391
FCM : anti-mouse IFNγ APC (rat monoclonal XMG1.2)	BioLegend	Cat# 505810; RRID: AB_315404
FCM : anti-mouse GZMB PE (rat monoclonal NGZB)	ThermoFisher	Cat# 12-8898-82; RRID: AB_10870787
FCM : anti-mouse Ki-67 BV605 (rat monoclonal 16A8)	BioLegend	Cat# 652413; RRID: AB_2562664
FCM : anti-mouse TNFα FITC (rat monoclonal MP6-XT22)	ThermoFisher	Cat# 11-7321-82; RRID: AB_465418
FCM: Zombie NIR™Fixable Viability Dye	BioLegend	Cat# 423105
FCM: Human TruStain FcX™ (Fc Receptor Blocking Solution)	BioLegend	Cat# 422302; RRID: AB_2818986
FCM: Purified Rat Anti-Mouse CD16/CD32 (Mouse Fc Block™) (rat monoclonal 2.4G2)	BD	Cat# 553142; RRID: AB_394657
InVivoMAb anti-mouse CD276 (B7-H3, rat monoclonal MJ18)	Bio X Cell	Cat# BE0124; RRID: AB_10950149
InVivoMAb rat IgG1 isotype control, anti-horseradish peroxidase (clone HRPN)	Bio X Cell	Cat# BE0088; RRID: AB_1107775
InVivoMAb anti-mouse CD8a (rat monoclonal 2.43)	Bio X Cell	Cat# BE0061; RRID: AB_1125541
InVivoMAb rat IgG2b isotype control, anti-keyhole limpet hemocyanin (clone LTF-2)	Bio X Cell	Cat# BE0090; RRID: AB_1107780
InVivoMAb anti mouse PD-1 (rat monoclonal RMP1-14)	Bio X Cell	Cat# BE0146; RRID: AB_10949053
InVivoMAb rat IgG2a isotype control, anti-trinitrophenol (clone 2A3)	Bio X Cell	Cat# BE0089; RRID: AB_1107769
Biological samples		
Non-tumor and brain metastasis tissue	Centre Hospitalier Universitaire Vaudois, Lausanne, Switzerland	NA

(*Continued on next page*)

Continued

REAGENT or RESOURCE	SOURCE	IDENTIFIER
Chemicals, peptides, and recombinant proteins		
Trizol (TRI Reagent) LS	Sigma-Aldrich	Cat# T3934
Tween® 20 for molecular biology	Applied Chemicals	Cat# A4974
Triton X-100	Applied Chemicals	Cat# A4975
2-Methylbutane	Sigma-Aldrich	Cat# 59070
Paraformaldehyde (PFA) 32% solution, EM grade	Electron Microscopy Sciences	Cat# 15714-S
Sodium phosphate dibasic (Na_2HPO_4)	Sigma-Aldrich	Cat# S5136
Sodium Phosphate Monobasic, Dihydrate ($NaH_2PO_4 \cdot 2H_2O$)	JT Baker	Cat# JTB-3819-01
L-Lysine	Sigma-Aldrich	Cat# 62840
Methanol, 99.9%	Thermo Fisher	Cat# 176840025
Collagenase/Dispase®	Sigma-Aldrich	Cat# 10269638001
Fetal Bovine Serum (FBS)	Gibco, ThermoFisher	Cat# 10270106
DNase I	Sigma-Aldric	Cat# 11284932001
Percoll®	Sigma-Aldric	Cat# P1644-100ML
Bovine Serum Albumin	Jackson ImmunoResearch	Cat# 001-000-162
Tissue-Tek® O.C.T. Compound	Sakura Finetek	Cat# 4583
Donkey Serum	Sigma Aldrich	Cat# S30-M
Fluorescence Mounting Medium	Dako	Cat# S302380-2
Pentobarbital	CHUV	NA
D(+)-Sucrose for molecular biology	PanReac AppliChem	Cat# A2211,1000
DMEM/F-12, GlutaMAX™ Supplement	Gibco, ThermoFisher	Cat# 31331028
Penicillin-Streptomycin (10,000 U/mL)	Gibco, ThermoFisher,	Cat# 15140122
Gadovist (Gadobutrol)	Bayer	NA
Tamoxifen, ≥99%	Sigma-Aldrich	Cat# T5648
Ganciclovir	InvivoGen	Cat# sud-gcv
UltraPure™ 0.5M EDTA	Invitrogen, ThermoFisher	Cat# 15575020
RBC Lysis Buffer (10X)	BioLegend	Cat# 420301
Trypan Blue Solution, 0.4%	Gibco, ThermoFisher	Cat# 15250061
Brilliant Stain Buffer	BD	Cat# 563794
Trypsin-EDTA (0.05%), phenol red	Gibco, ThermoFisher	Cat# 25300062
Attane™ Isoflurane	Attane	NA
Sunflower seed oil from *Helianthus* annuus	Sigma-Aldrich	Cat# S5007-250ML
Critical commercial assays		
Chromium Next GEM Single Cell 3' Kit v3.1	10x genomics	Cat# 1000268
Dual Index Kit TT Set A, 96 rxns	10x genomics	Cat# 1000215
Chromium Next GEM Chip G Single Cell Kit	10x genomics	Cat# 1000127
Library Construction Kit	10x genomics	Cat# 1000190
Qubit dsDNA HS Assay Kit	ThermoFisher	Cat# Q32851
Tumor Dissociation Kit, mouse	Milteny	Cat# 130-096-730
Deposited data		
scRNA-seq (human) and RNA-seq (human, mouse) count data	This paper	Database: https://joycelab.shinyapps.io/braintime/
RNA-seq mouse raw data	This paper	Database: https://www.ncbi.nlm.nih.gov/geo/query/acc.cgi?acc=GSE228355
Human reference genome (GRCh38.p13, Sept 2020)	Gencode	https://www.gencodegenes.org/human/release_36.html
Mouse reference genome (GRCm39, Jan 2021)	Gencode	https://www.gencodegenes.org/mouse/release_M26.html

(*Continued on next page*)

Continued

REAGENT or RESOURCE	SOURCE	IDENTIFIER
Experimental models: Cell lines		
PyMT-BrM3 (breast-BrM)	Joyce lab (Croci et al.[62])	NA
Sv2T3-BrM1 (lung-BrM)	Joyce lab	NA
Yumm1.1-BrM4 (melanoma-BrM)	Joyce lab (Saltarin et al.[63])	NA
Experimental models: Organisms/strains		
Mouse: PDGFRβ-P2A-CreERT[2] (C57BL/6J background)	Jackson Laboratories	IMSR_JAX:030201
Mouse: Rosa26-LSL-tdTomato	Joyce Lab	NA
Mouse: PDGFRβ-TK	Jackson Laboratories	IMSR_ JAX: 029924
Software and algorithms		
GraphPad Prism (version 8.1.0)	GraphPad software	https://www.graphpad.com/scientific-software/prism/
FlowJo (version 10.7.2)	BD Biosciences	https://www.flowjo.com/
R (version 4.2.2)	The R Foundation	https://cran.r-project.org/
QuPath (version 0.3.0)	Bankhead et al.[64]	https://qupath.github.io/
Visiopharm (version 2022.04)	Visiopharm software	https://visiopharm.com/
STAR (v2.7.9a)	Dobin at al.[65]	https://github.com/alexdobin/STAR
RSEM (v1.3.3)	Li et al.[66]	https://github.com/deweylab/RSEM
biomaRt (R package, version 2.50.3)	Bioconductor	https://bioconductor.org/packages/release/bioc/html/biomaRt.html
Tximport (R package, version 1.22.0)	Bioconductor	https://bioconductor.org/packages/release/bioc/html/tximport.html
sva (R package, version 3.42.0)	Bioconductor	https://bioconductor.org/packages/release/bioc/html/sva.html
limma (R package, version 3.50.3)	Bioconductor	https://bioconductor.org/packages/release/bioc/html/limma.html
edgeR (R package, version 3.36.0)	Bioconductor	https://bioconductor.org/packages/release/bioc/html/edgeR.html
clusterProfiler (R package, version 4.2.2 and 3.18.1)	Bioconductor	https://bioconductor.org/packages/release/bioc/html/clusterProfiler.html
msigdbr (R package, version 7.5.1)	Bioconductor	https://bioconductor.org/packages/release/data/experiment/html/msigdb.html
org.Hs.eg.db (R package, version 3.12.0 and 3.14.0)	Bioconductor	https://bioconductor.org/packages/release/data/annotation/html/org.Hs.eg.db.html
org.Mm.eg.db (R package, version 3.12.0)	Bioconductor	https://bioconductor.org/packages/release/data/annotation/html/org.Mm.eg.db.html
Seurat (R package, version 4.1.0)	Hao, Hao et al.[67]	https://github.com/satijalab/seurat
STACAS (R package, version 2.0.1)	Andreatta et al.[68]	https://github.com/carmonalab/STACAS
Corrplot (R package, version 0.92)	Taiyun Wei and Viliam Simko, 2021	https://github.com/taiyun/corrplot
scmap (R package, version 1.14.0)	Kiselev et al.[35] Bioconductor	https://bioconductor.org/packages/release/bioc/html/scmap.html
UCell (R package, version 1.3.1)	Andreatta et al., 2022	https://rdrr.io/github/carmonalab/UCell/
ggcorrplot (R package, version 1.1.4)	NA	https://cran.r-project.org/web/packages/ggcorrplot/ggcorrplot.pdf
Other		
gentleMACS™ Octo Dissociator with Heaters	Miltenyi	Cat# 130-096-427
gentleMACS™ C Tubes	Miltenyi	Cat# 130-096-334

(*Continued on next page*)

Continued

REAGENT or RESOURCE	SOURCE	IDENTIFIER
MoFlo Astrios EQ	Beckman Coulter	NA
BD FACSAria™ II	BD	NA
Axio Scan.Z1 slide scanner	Zeiss	NA
Qubit™ 4 Fluorometer	Invitrogen, ThermoFisher	Cat# Q33238
Tissue-Tek® Cryomold® Standard	Sakura Finetek	Cat# 4557
Rectangular cover glasses	Menzel Gläser, VWR	Cat# 631-1339
Multifly® needle, 25G x 3/4'', 80 mm	Sarsted	Cat# 85.1642.005
LSRFortessa flow cytometer	BD	NA

RESOURCE AVAILABILITY

Lead contact

Further information and requests for resources should be directed to and will be fulfilled by the lead contact, Prof. Johanna A. Joyce (johanna.joyce@unil.ch).

Materials availability

This study did not generate new unique reagents.

Data and code availability

RNA-seq (human and mouse) and scRNA-seq (human) count expression data generated during this study can be visualized and downloaded at: https://joycelab.shinyapps.io/braintime/.

Mouse raw RNA-seq data is also available at: https://www.ncbi.nlm.nih.gov/geo/query/acc.cgi?acc=GSE228355.

Due to strict patient privacy protection regulations, human raw sequencing data cannot be deposited in a public repository. Requests for access to the raw human single cell and bulk RNA-seq data must be made to the lead contact for subsequent referral to the institutional ethics committee. Future users can contact the corresponding author for access to the raw, unprocessed RNA-seq data, and those requests will then be individually reviewed by the relevant institutional committees. This paper does not report any original code.

EXPERIMENTAL MODEL AND STUDY PARTICIPANT DETAILS

Human subjects

All experimental procedures performed on clinical human tissue samples were in accordance with the ethical standards of the institutional and/or national research committees and with the 1964 Helsinki declaration and its later amendments or comparable ethical standards. All participants included in this study provided an informed consent. The collection of tumor tissue and blood samples at the Biobank of the Brain and Spine Tumor Center (BB_031_BBLBGT) of the Centre Hospitalier Universitaire Vaudois (CHUV, Lausanne, Switzerland) was approved by the Commission Cantonale d'éthique de la recherche sur l'être humain (CER-VD, protocol PB 2017-00240, F25 / 99). Tissue samples were immediately collected after surgery, anonymized, and processed as described below. Pathological review of tumor tissues was performed at CHUV as part of the standard clinical care; all clinical information is included in Table S1.

Mouse models

All animal studies were approved by the Institutional Animal Care and Use Committees of the University of Lausanne and Canton Vaud, Switzerland (License numbers: VD3314 and VD3688). Mice were housed in the Agora *In Vivo* Center (AIVC) animal facility in individually ventilated cages, under a 12h light/dark schedule at 22°C and in the presence of 2-4 cage mates. Standard autoclaved lab diet and water were provided *ad libitum*.

PDGFRβ-P2A-CreERT[2] mice were purchased from Jackson Laboratories (C57BL/6J background, JAX: 030201) and crossed with Rosa26-LSL-tdTomato[69] mice (C57BL/6J background) to generate PDGFRβ-CreERT2-R26Tom mice. C57BL/6J mice were purchased from Charles River Laboratories. PDGFRβ-TK mice were purchased from Jackson Laboratories (C57BL/6J background, JAX: 029924). Littermates of the same sex were randomly assigned to the experimental groups.

Cell lines

For BrM induction (see section ''Generation of experimental brain metastases''), the cell lines PyMT-BrM3 (breast-BrM), Sv2T3-BrM1 (lung-BrM) and Yumm1.1-BrM4 (melanoma-BrM) were used. The three cell lines were cultured in DMEM-F12 (1:1) +Glutamax (Gibco) containing 10% fetal bovine serum (FBS, Gibco) and 1% penicillin/ streptomycin (Gibco). PyMT-BrM3 and Yumm1.1-BrM4 were

grown under adherent conditions. The Sv2T3-BrM1 cell line was maintained under adherent conditions until 12h prior to injection; at this point, cells were then cultured in 30 μl hanging drops in an inverted plate.

The PyMT-BrM3 breast cell line was derived from the murine parental 99LN cell line, which was isolated from a metastatic lymph node lesion that arose in the MMTV-PyMT (murine mammary tumor virus; polyoma middle T antigen) breast cancer model (C57BL/6J background). This cell line was sequentially selected three times *in vivo* for brain-homing capacity, resulting in the PyMT-BrM3 variant[62] used herein. The Yumm1.1-BrM4 melanoma line was established by subjecting the parental Yumm.1.1 cell line[70] to four rounds of *in vivo* selection.[63] The same approach was used to generate the Sv2T3-BrM1 cell line after one round of *in vivo* passaging of a parental line derived from the $Kras^{LSL\text{-}G12D/WT}$;$p53^{fl/fl}$ (KP) lung cancer model.[71] The breast PyMT-BrM3 model mimics all the later stages in the metastatic cascade, from cancer cell dissemination in the bloodstream to the seeding and outgrowth of multiple metastases in the brain parenchyma. Yumm1.1-BrM4 cells can only be used to model the initial stages of BrM (micrometastasis), due to the outgrowth of cancer cells at the injection site. The Sv2T3-BrM1 cell line also leads to the growth of multiple metastases in the brain parenchyma, which are more frequently accompanied by meningeal and extracranial tumors.

METHOD DETAILS

Endothelial cell and mural cell isolation using fluorescence-activated cell sorting

Endothelial and mural cell isolation was adapted from a previous protocol.[57] Mouse metastases were first dissected out from the surrounding brain tissue before processing. Briefly, human or mouse tissue was minced for less than 5 minutes (min). The pieces were transferred into a gentleMACS digestion tube (Milteny) containing collagenase/dispase (3.3 mg/ml, Sigma-Aldrich) in 2% FBS and incubated in a gentleMACS Octo Dissociator (Miltenyi) at 37°C for 30 min with gentle rocking. The tissue was spun down at 300g to form a pellet and mechanically dissociated with 1ml of DNAse (0.5 mg/ml, Sigma-Aldrich) in 2% FBS (Gibco) using a p1000 pipet. For myelin removal, the sample was transferred to a tube containing 4 ml of 22% Percoll solution (Sigma-Aldrich) and centrifuged 10 min at 560g without the break on. After centrifugation the supernatant was removed, and the sample was incubated with red blood cell (RBC) lysis buffer (BioLegend) for 10 min. The suspension was then washed with PBS (Gibco) and transferred to a FACS tube to proceed with the staining. The cell suspension was stained with Zombie NIR fixable viability die (BioLegend) for 20 min, followed by blocking with Human TruStain FcX Fc receptor blocking solution (BioLegend) to block human samples, or Purified Rat Anti-Mouse CD16/CD32 (BD) to block mouse samples, for 10 min. The antibody mix (see key resources table) was incubated for 15 min in the dark. After incubation, the samples were washed and resuspended in FACS buffer containing 0.5% bovine serum albumin (BSA, Jackson ImmunoResearch) and 2 mM EDTA (Invitrogen) to proceed with the cell sorting. Cell sorting was performed using the multicolor fluorescence-activated cell sorter (BD FACSAria or MoFlo Astrios EQ). For human samples, we gated on $Zombie^-$ $CD45^-$ $CD11B^-$ cells to discard dead and immune cells (i.e. $Zombie^+$ $CD45^+$ $CD11B^+$ cells), followed by $CD31^+$ gating for ECs or $PDGFR\beta^+$ gating for mural cells. Cells were sorted into Trizol LS (Sigma Aldrich) for bulk RNA-seq or in 2 ml tubes with 2 μl of HBSS (Gibco) for scRNA-seq. For mouse samples, we gated on the $Zombie^-$ $CD45^-$ $CD11b^-$ $Epcam^-$ cells to discard dead, immune, and cancer cells (i.e. $Zombie^+$ $CD45^+$ $CD11b^+$ $Epcam^+$ cells), followed by $CD31^+$ gating for ECs or $PDGFR\beta^+$ gating for mural cells. Cells were sorted into Trizol LS (Sigma Aldrich) for bulk RNA-seq.

In addition, wherever possible, flow cytometry analysis was performed in parallel for the same human samples to quantify different immune cell populations.[8,11–13] This allowed us to integrate the information regarding immune cell proportions with the transcriptomic and functional analyses of the vasculature in matched samples.

Single-cell RNA-sequencing

Samples were processed using the Chromium Next GEM Single Cell 3' Reagent Kits v3.1 (Dual Index, 10x Genomics). Libraries were quantified by a fluorometric method (Qubit, Thermo Fisher) and their quality was assessed on a Fragment Analyzer (Agilent Technologies) in the Lausanne Genomic Technologies Facility (GTF) operated by the University of Lausanne. Samples were sequenced in the GTF using the NovaSeq 6000.

Mapping was performed using CellRanger (v 6.0.1) with default parameters on the human reference transcriptome refdata-gex-GRCh38-2020-A. Count matrices were imported into R (v 4.0.5) and subsequently analyzed using the Seurat package[67] (v 4.1.0). For ECs, count matrices were filtered to retain cells bearing (i) between 400 and 4,200 genes, (ii) between 0.5% and 20% of mitochondrial gene counts, (iii) between 5% and 25% of ribosomal protein-encoding gene counts and (iv) less than 14,000 total RNA molecules. A minority of cells (~5.5%) with low *PECAM1* expression and expression of immune cell markers (*PTPRC)* or cancer stem cell markers (*KRT19, CD24*) were excluded. ECs from one BrM sample (156) were excluded due to a very low cell number of cells (<100). For mural cells, count matrices were filtered to retain cells bearing (i) between 800 and 5,000 genes, (ii) between 0.5% and 20% of mitochondrial gene counts, (iii) between 5% and 25% of ribosomal protein-encoding gene counts and (iv) less than 20,000 total RNA molecules. A minority of cells (~1.2%) with low expression of *PDGFRB,* and expression of other markers such as the stem cell markers *KRT19* or *CD24,* were excluded. Genes detected in less than 5 cells were not considered for downstream analyses, resulting in a final set of 10,045 cells and 22,524 genes for EC samples, and of 29,798 cells and 24,885 genes for mural cell samples. Gene counts were normalized using the NormalizeData function with default parameters, which normalizes the gene expression measurement for each cell by the total expression of that cell, multiplies the obtained value by a scale factor, and natural-log transforms the result. Most variable genes detection and sample integration were performed through the STACAS[68] package (v 2.0.1). Principal component (PC) analysis was computed with the RunPCA function and cell clustering was performed using the shared nearest

neighbor modularity optimization–based algorithm implemented in the functions FindNeighbors and FindClusters, based on the first 30 PCs. UMAP dimensionality reduction was derived through the RunUMAP function based on the first 30 PCs. Genes differentially expressed between clusters were determined using the FindAllMarkers function, using the parameters min.pct = 0.25 and only.pos = TRUE. We used published markers[28,31–33,72] to identify the already known endothelial or mural cell subtypes: arteries, veins, capillaries, pericytes, SMCs, and fibroblasts. The remaining clusters were named based on the top DEGs. Genes with p.adj < 0.01 and a logfc.threshold = 0.25 of expression level between the cluster of interest versus the other clusters were kept for the ORA analysis, executed through clusterProfiler[73] (v 3.18.1). Violin plots are based on the normalized expression values for selected genes. Dotplots display scaled values for selected genes, obtained through the ScaleData function with default parameters, together with the percentage of cells in each population where the gene of interest is detected. UMAP plots highlighting specific gene signatures rely on the relevant signature score generated through the function AddModuleScore using default settings.

To integrate our scRNA-seq data with reference single-cell datasets, we used STACAS R package (v 2.1.0). Integration was performed following log transformation of raw counts and was based on the top 1,000 anchor features and the first 20 PCs. For Garcia et al. *Nature* (2022),[31] the data was downloaded at http://compbio.mit.edu/scBBB/ and selected cells were annotated as either endothelial or mural cells. Specifically, for the integration with our data, we used their dataset from post-mortem pathologically normal donor samples across seven different brain regions as part of the Religious Orders Study and Rush Memory and Aging Project (ROSMAP) cohort.[74] For Geldhof et al. *Nat. Commun*. (2022),[36] the data was downloaded through the gene expression omnibus database (accession code GSE155109). We discarded peri-tumoral cells or cells with low sequencing counts. For Goveia et al. *Cancer Cell* (2020),[37] the data was downloaded through the Lung ECTax database at https://endotheliomics.shinyapps.io/lung_ectax/. We only considered those cells that had been annotated as tumor ECs (“TEC”). Following integration, we performed dimensional reduction (UMAP) using standard functions from the Seurat R package (RunUMAP). To compute the transcriptomic similarity between our data and the reference cell groups, we computed the correlation between average gene expression per group. The resulting Spearman’s rho statistic was used as a rank-based measure of association. To label cells from reference datasets according to our cluster labels, we used the unsupervised method for projection implemented in the *scmap* R package (v 1.14.0). Projection was based on the top 1,000 most informative features (SelectFeatures function). We did not impose any threshold on the similarity scores.

Bulk RNA-sequencing

Mouse and human endothelial and mural cell populations were sorted into Trizol LS (Sigma Aldrich, cat. no. T3934) and submitted to the company “GeneWiz from Azenta Life Sciences” for RNA extraction, quality control analysis, library preparation, and sequencing. Total RNA was extracted from cells following the Trizol Reagent User Guide (Thermo Fisher Scientific) and quantified using Qubit 2.0 Fluorometer (Life Technologies, Carlsbad, CA, USA). Agilent TapeStation 4200 (Agilent Technologies, Palo Alto, CA, USA) was used to assess RNA integrity. cDNA synthesis and amplification were performed with the SMART-Seq HT Ultra Low Input Kit for Sequencing (Clontech, Mountain View, CA), and Illumina Nextera XT library was used for sequencing library preparation, following the manufacturer’s instructions. Paired-end 150 base-pair (2x150) sequencing of the libraries was performed using the Illumina NovaSeq 6000 or Illumina Hiseq 3000/4000 sequencers.

Alignment of RNA-seq reads was performed using STAR[65] (v 2.7.9a) and quantified using RSEM[66] (v 1.3.3). Human genome version 38 was used with GENCODE v36 annotation. Murine genome version 39 was used with GENCODE M26 annotation. Samples with a library size < 2.10^6 were excluded from the analysis (human NorCor37-PDGFRβ; murine 53142-PDGFRβ and 51697-PDGFRβ). FPKM and raw counts of transcripts with the same gene symbol were pooled. Non-protein coding genes, pseudogenes, predicted genes, predicted pseudogenes, and genes with 0 FPKM in all samples were filtered out. A total of 18,917 genes for human and 18,665 genes for mouse were retained and their expression was normalized between samples using the TMM method (edgeR[75] v 3.36.0) and log2 transformed with voom (limma[76] v 3.50.3). When applicable, batch effect was corrected with ComBat (sva[77] v 3.42.0). Differential expression was computed using limma.[76] Genes with p.adj value <0.05 and -1>LFC>1 were called significantly differentially expressed in all comparisons. Pathway analyses (ORA and GSEA) were performed using clusterProfiler[73] R package (v 4.2.2). Pathways with p.adj value <0.05 were considered statistically significant. Gene signature single sample scores were computed with the combined z-score method (*hacksig* R package v 0.1.2) using the top 20 marker genes, the BBB dysfunction module gene signature,[39] or interferon signatures from Hallmark, Reactome, and GOBP databases. Pearson’s correlation was computed between single sample scores and the proportions of specific immune cell infiltrates in each sample using ggcorrplot (R package, v 1.1.4).

For the application of gene signatures from our bulk RNA-seq data to public scRNA-seq datasets, we first downloaded the datasets from the different databases. For Abdelfattah et al. *Nat. Commun.* (2022),[44] raw count data was downloaded through the gene expression omnibus database (accession code GSE182109). Metadata was downloaded through GitHub at https://github.com/parveendabas/GBMatlas/blob/master/Meta_Data_GBMatlas.txt. For Jerby-Arnon et al. *Cell* (2018),[43] data was downloaded through the Broad Institute Single Cell portal at https://singlecell.broadinstitute.org/single_cell/study/SCP109. For Wu et al. *Nature Genetics* (2021),[41] data was downloaded through the Broad Institute Single Cell portal at https://singlecell.broadinstitute.org/single_cell/study/SCP1039. For Salcher et al. *Cancer Cell* (2022),[42] data was downloaded from the Single-cell Lung Cancer Atlas at https://luca.icbi.at/. In order to have an internal control, we integrated our scRNA-seq data and the reference public datasets following the procedure explained in the previous section for the scRNA-seq integration. Following integration, dimensionality reduction and unsupervised clustering were performed using standard functions from the Seurat R package (RunUMAP, FindNeighbors and FindClusters, using the first 20 principal components). We checked the expression of known endothelial and mural cell markers, and selected clusters of cells that corresponded closely with the endothelial and mural cells from our datasets. We then repeated the integration procedure

but using these selected cell clusters only. Following data integration, we used the top 50 markers from our RNA-seq data (differentially expressed genes with p.adj value <0.05 and -1>LFC>1, when comparing each BrM subtype versus the two others) to create breast-, lung- and melanoma-BrM EC cell signatures. We computed signature scores in our integrated data using the AddModuleScore_Ucell function (Seurat R package). After scaling to a range between 0 and 1, we used these scores used as a similarity measure between our RNA-seq cell groups and public scRNA-seq references.

Immunofluorescence staining

Clinical samples were OCT-embedded (Sakura Finetek) by submersion in cold 2-methyl butane (Sigma-Aldrich) and stored at -80°C. Tissue blocks were sectioned at 10 μm thickness and mounted on glass slides. The tissue was air-dried and fixed in cold 100% methanol (Thermo Fisher). Sections were rehydrated with PBS (Gibco) 1x, permeabilized with 0.2% TritonX-100 (Applied Chemicals) in PBS for 3h at room temperature (RT), and blocked with 10% normal donkey serum (NDS) (Sigma-Aldrich) in PBS for a minimum of 1h at RT. After removal of the blocking buffer, the tissue was incubated with the primary antibody mix (see key resources table) overnight at 4°C. After washing 3 times (10 min each) with 0.2% Tween (Applied Chemicals) in PBS on a shaker at RT, the slides were incubated with the secondary antibody mix (see key resources table) and DAPI (Invitrogen) for 1h at RT. The tissue was then washed 3 times (10 min each) with 0.2% Tween-20 in PBS on a shaker at RT and incubated with the conjugated antibody mix if applicable for 1h at RT. In the last step, the slides were washed again 3 times (10 min each) with 0.2% Tween in PBS on a shaker at RT, mounted using Dako fluorescence mounting medium (Agilent), and covered with a coverslip. Sections were imaged on an Axio Scan.Z1 slide scanner (Zeiss) using a 20x objective.

Mice were sacrificed by terminal anesthesia using pentobarbital, followed by intracardiac perfusion with PBS and periodate-lysine-paraformaldehyde (PLP) buffer. Brains were dissected and incubated in PLP for 24h at 4°C and in 30% sucrose for an additional 24h at 4°C. The tissue was then embedded in OCT, stored at -80°C, sectioned at a thickness of 10 μm, and mounted on slides. Sections were permeabilized with 0.2% TritonX-100 in PBS for 30 min at RT and blocked with 10% NDS in PBS for a minimum of 1h at RT. Antibody incubations (see key resources table) were performed as explained above for the human sections. Sections were scanned on an Axio Scan.Z1 slide scanner (Zeiss) using a 20x objective.

Image analysis

Image analysis was performed using the VIS Image Analysis software (Visiopharm) or QuPath[64] (v 0.3.0) image analysis software.

Visiopharm analysis: for each sample, a region of interest (ROI) was manually defined to exclude tissue edges and aberrant signals (i.e. those resulting from tissue folds, dust particles, or air bubbles). Object classification was performed by setting detection thresholds based on pixel intensity.

Qupath analysis: for each sample, a ROI was manually defined to exclude tissue edges and aberrant signals (i.e. those resulting from tissue folds, dust particles, or air bubbles). The StarDist method[78] was used for nuclear segmentation, powered by the dsb2018_heavy_augment.pb deep learning model with the following parameters: threshold = 0.5; channels = 'DAPI'; pixelSize = 0; cellExpansion = 3; cellConstrainScale = 1.5; measureShape = true; measureIntensity = true; includeProbability = true; nThreads = 10. Object classification was performed by setting detection thresholds based on pixel intensity.

Generation of experimental brain metastasis

For breast- or melanoma-BrM generation in immunocompetent mice, $1x10^5$ PyMT-BrM3 cells or $50x10^3$ Yumm1.1-BrM4 cells respectively were inoculated into the left cardiac ventricle of 6-10 weeks old C57BL/6J, PDGFRβ-CreERT2-R26Tom and/or PDGFRβ-TK mice. Cells were counted and resuspended in HBSS (Gibco) in the corresponding concentration.

For lung-BrM generation in immunocompetent mice, cells were resuspended at a concentration of 67000 cells/ml and seeded in drops of 30 μl in the lid of a Petri dish. The lid was then inverted, and cells were incubated for 12h before injection to allow for the formation of hanging spheres. During the incubation time, PBS was added to the Petri dish to prevent evaporation. Four Sv2T3-BrM1 hanging drops per mouse were inoculated into the left cardiac ventricle of 6-10 weeks old C57BL/6J or PDGFRβ-CreERT2-R26Tom mice.

To minimize the outgrowth of melanoma or lung cancer cells in the injection site, the direct injection of the cancer cells into the heart was avoided. Instead, a Multifly-needle (25G, 80mm, SARSTED) with an attached syringe filled with PBS was inserted in heart, followed by cancer cell injection into the catheter tube and a flush with PBS.

Mouse monitoring by magnetic resonance imaging (MRI)

Mice were monitored by weekly MRI using a 3 Tesla small animal MR scanner (Bruker BioSpin MRI, Ettlingen, Germany) with an 82-mm volume coil as a transmitter combined with a 2 × 2 mouse brain phased array surface coil for signal reception.

Mice were anesthetized with 2.5% isoflurane (Attane) in oxygen for 1–2 min and injected with 150 μl of gadolinium (Gadovist, 1 mmol/ml, Bayer). Data acquisition was performed using Paravision 360 v2.0 software (Bruker BioSpin MRI, Ettlingen, Germany). A 3-slice localizer was used to assess the mouse head position, followed by a T1-FLASH (fast low-angle shot magnetic resonance) sequence with the following parameters: repetition time (TR) = 232.9 ms, echo time (TE) = 5.2 ms, flip angle = 50°, number of averages (NA) = 4, number of slices = 9, slice thickness (ST) = 0.7 mm, field of view (FOV)= 20x20 mm^2, matrix size (MS) = 128 × 128, pixel size 0.156 × 0.156 mm^2, acquisition time (Tacq) = 1m33s with images being acquired in axial planes. Anesthesia was maintained throughout the whole procedure. The body temperature was kept constant at 37.0±0.5°C with a tubing system circulating warm

water, while the respiration rate was monitored using a respiration pillow placed below the mouse abdomen (SA Instruments, Stony Brook, New York, USA). MIPAV software (National Institutes of Health, USA) was used to measure tumor volume. Mice were sacrificed when symptomatic.

Measuring blood-brain barrier leakage using gadolinium enhanced MRI

BBB leakage was calculated based on the changes in T1 relaxation time values pre- vs. post-gadolinium injection as previously described.[49] The reduction in T1 value following gadolinium administration is an indicator of BBB leakage. Mice were anesthetized with 2.5% isoflurane (Attane) in oxygen for 1–2 min and a Multifly-needle (25G, 80mm, SARSTED) was placed in the peritoneum. Once the needle was inserted, the catheter was fixed to the skin using surgical tape. All MRI experiments were performed on a 3 Tesla small animal MR scanner (Bruker BioSpin MRI, Ettlingen, Germany). The anesthesia was maintained for the duration of the MR protocol. The body temperature was kept constant at 37.0±0.5°C with a tubing system circulating warm water, while the respiration rate was monitored with a respiration pillow placed below the mouse abdomen (SA Instruments, Stony Brook, New York, USA). A three-plane low-resolution localizer scan was performed for anatomic localization and then a rapid acquisition with relaxation enhancement (RARE) T1-map scan was acquired pre- and post-contrast injection. Mice were injected with gadolinium at 0.2 mg/kg concentration and the post-contrast images were acquired 5 min post-injection. The RARE pulse sequence parameters were as follows: TR = 420, 500, 700, 1500, 3000, 9000 ms, TE = 16.3 ms, RARE factor = 4, FOV= 20x20 mm^2, matrix size (MS) = 128 × 128, pixel size = 0.156 × 0.156 mm^2, number of slices = 9, ST = 0.7 mm, Tacq = 8m4s. All image analyses were performed in MatLab (MathWorks, Natick, Massachusetts, USA). Pixel-wise T1-mapping was performed by fitting a mono-exponential curve to the signal intensities of the six T1-weighted RARE-images using the least-squares method.

The fitting model used in this study is the following:

$$S = S0 * (1 - \exp(-TR / T1))$$

where S0 is the signal when TR is long compared to T1.

The post-injection image with TR = 420 ms was chosen for segmentation and very inclusive ROIs were drawn around the tumor. T1 maps were calculated pre- and post-injection and subsequently, in order to determine the change of tumor T1 due to gadolinium injection, ΔT1 maps were obtained (in percentage) by dividing the post-injection map by the pre-injection map, then subtract 1, and multiply by 100.

Mouse treatments

Tamoxifen treatments: tamoxifen (Sigma-Aldrich) was diluted with sunflower seed oil (Sigma-Aldrich) to create a stock of 10mg/ml. To induce recombination, PDGFRβ-CreERT2-R26Tom BrM-bearing mice (or healthy mice used as control) received 2mg of tamoxifen daily for 5 consecutive days.[45]

Ganciclovir treatments*:* ganciclovir (InvivoGen) was prepared according to the manufacturer's instructions. To induce mural cell depletion, PDGFRβ-TK BrM-bearing mice were treated with ganciclovir daily at a concentration of 75 mg/kg until the end of the experiment.

αCD276 treatments: anti-mouse CD276 antibody (B7-H3, Clone MJ18) and the corresponding isotype control (rat IgG1) were obtained from InVivoMab (BE0124 and BE088). Following BrM detection by MRI, mice received intraperitoneal injections of either 300 μg of αCD276 or the isotype control every other day until the end of the experiment.

αCD8 treatments: anti-mouse CD8a (clone 2.43) and the corresponding isotype control (rat IgG2b) were obtained from InVivoMab (BE0061 and BE0090). Following BrM detection by MRI, mice received intraperitoneal injections of 500 μg (first dose) and 250 μg (remaining doses) of αCD8a or the isotype control twice per week until the end of the experiment.

αPD-1 treatments: anti mouse PD-1 (clone RMP1-14) and the corresponding isotype control (rat IgG2a) were obtained from InVivoMab (BE0146 and BE089). Following BrM detection by MRI, mice received intraperitoneal injections of either αPD-1 or the isotype control at a concentration of 10 mg/kg twice per week until the end of the experiment.

Flow cytometry analysis of T cell phenotype

Mice were injected with 250 μg Brefeldin A (Sigma) 6h prior to sacrifice and sacrificed by terminal anesthesia using pentobarbital, followed by intracardiac perfusion with PBS. Tumors were dissected, minced for < 5 min and digested using the mouse tumor dissociation kit (TDK) in a gentleMACS Octo Dissociator (Miltenyi). As recommended by the manufacturer, a reduced amount of enzyme R (10 μl) was used to ensure the preservation of cell surface epitopes. The digested tissue was then centrifuged at 300g to form a pellet, filtered and incubated with RBC lysis buffer (BioLegend) for 5 minutes. The cell suspension was then washed with PBS (Gibco) and frozen in FBS with 10% DMSO. Following collection of all the samples, the cell suspensions were thawed and transferred to a U bottom 96 well plate. All samples were stained in parallel with Zombie NIR fixable viability dye (BioLegend) for 20 min, followed by blocking with Purified Rat Anti-Mouse CD16/CD32 (BD) for 10 min. The extracellular antibody mix (see key resources table) was incubated for 15 min in the dark. After incubation, the samples were washed and fixed with 200 μl of 1x Fix solution from the True-Nuclear Transcription Factor Buffer Set (BioLegend) for 1h, followed by 3 washes with 200 μl of 1x Perm buffer. The intracellular antibodies were incubated overnight at 4C in 1x Perm buffer. The following morning, the samples were washed 3 times with 1x Perm buffer and resuspended in FACS buffer containing 0.5% BSA (Jackson ImmunoResearch) and 2 mM EDTA (Invitrogen) to proceed with the acquisition using a 5-Laser LSRFortessa flow cytometer (BD). Analysis was performed using FlowJo software (BD). Cells were gated on

Zombie^{-}CD45^{+}CD11B^{-}TCRβ^{+}CD8^{+} to select CD8^{+} T cells, which were then analyzed for the expression of TNFα, IFNγ, Ki-67, Granzyme B, CD44 and CD62L.

Statistical analysis

Statistical analyses were performed using GraphPad Prism software and the limma[76] and clusterProfiler[73] R packages (for assessing differential gene expression and GSEA/ORA, respectively). Summary data are presented as mean ± standard error of the mean (SEM), as indicated in the corresponding figure legends. Student's t-test and ordinary ANOVA were applied to continuous normal data; while the equivalent non-parametric Mann-Whitney and Kruskal-Wallis tests were used when data distributions failed normality tests. When multiple groups were compared, individual *P*-values were corrected for multiple testing using the Bonferroni correction method. For differential expression analysis and signature score correction, P-values were corrected for multiple hypothesis testing using the Benjamini-Hochberg procedure. Differences were considered statistically significant at $P \leq 0.05$ or $P.adj \leq 0.05$.